Absolute efficiency calibration of a NE-213 liquid scintillator using a ^{252}Cf source

A thesis submitted for the Degree of Master of Science

by

Martin Karlsson

Aug 29th, 1997

The Department of Nuclear Physics in Lund
Lund University Sweden

Absolute efficiency calibration of a NE-213 liquid scintillator using a ^{252}Cf source

Abstract

In a time-of-flight experiment, the absolute efficiency of a NE-213 liquid scintillator has been measured using a ^{252}Cf source. The neutrons emitted in the spontaneous fission of ^{252}Cf were measured in coincidence with a fission fragment. The total error involved in measuring the efficiency was ≈13%. The results have been compared to Stanton code simulations and the measured values are approximately 5 percentage units lower than the predictions of the Stanton code. Also measured was the transmission of neutrons through a 2 cm thick veto detector, with the result comparing well with GEANT simulations.

Contents

Chapter 1

Introduction

The purpose of this diploma work was to

- Determine the absolute efficiency of a NE-213 liquid scintillator using a ^{252}Cf source.
- Measure the neutron transmission in a thin veto detector.

The work was carried out within the Nuclear Physics group at Max-Lab in Lund. The group usually has 12 weeks a year of available beam time during which different research projects are carried out. The different projects do have one thing in common, they all use the tagged photons emitted as bremstrahlung when electrons, accelerated in a racetrack microtron, impinges on a radiator. The tagged photons further destiny depends on what experiment is undertaken.

During a seven day period in February/March 1995 a ^{4}He(γ,n) experiment was run in which the main objective was to obtain the absolute angular distribution of the cross section in question. The reason being the existence of some contradictory results and furthermore, the values of the cross section depend upon whether or not the nuclear force is charge symmetric. Thus, an accurate determination of the cross section governing the angular distribution will solve the discrepancy.

In the ^{4}He(γ,n) experiment, the neutrons were detected in one of two large neutron detectors shown in Fig. 1.1. The large neutron detector was constructed out of nine individual cells, all containing the liquid scintillator NE-213, and the detector used in our experiment was an exact copy of one of the nine individual cells.

In almost all experiments involving the determination of a distribution of fast neutrons, the factor introducing the largest error is usually the efficiency of the neutron detector and this is especially true for neutrons in the energy region 1-10 MeV, because at these energies, the cross sections involved in the neutron interaction with the scintillator are not as well defined as they are at higher energies. These cross

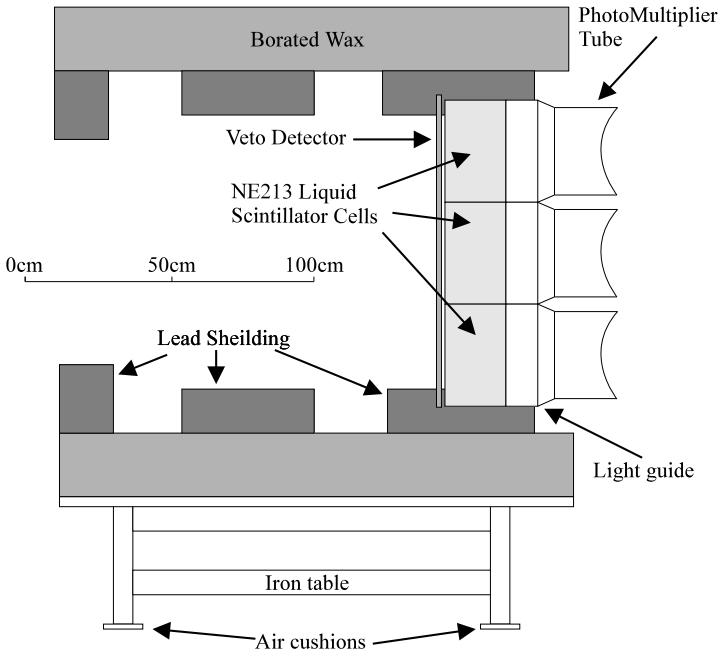

Figure 1.1: A picture of the large, 3 by 3, neutron detector used in the ^{4}He(γ,n) experiment. From [And 94].

sections are used when Monte Carlo simulations are carried out to calculate the efficiency, which is the usual procedure in determining the the efficiency. Thus the calculated efficiencies may not be accurate. In the ^{4}He(γ,n) experiment neutrons with energies down to as low as 2 MeV were detected.

The veto detector, a plastic NE-110 detector, can also be seen in front of the NE-213 detectors in Fig. 1.1. The reason for having a veto detector is to reject charged particles entering the NE-213, by using anti-coincidence methods, i.e. when a particle is detected in both the veto and the neutron detector it is most probably a charged particle and the event will be removed. However, the veto detector will of course also attenuate the neutron flux. This attenuation within the veto detector was also measured in this work.

The underlaying reasons for this diploma work are now clear.

Chapter 2

Neutron Detection

The general idea in neutron detection is to convert the uncharged neutrons into charged, and thereby directly detectable particles. Depending on the energy of the neutrons, several different methods for this conversion exist. For slow neutrons, many detectors are based on the, perhaps most popular, $^{10}\mathrm{B}(n,\alpha)^{7}\mathrm{Li}$ reaction. The net energy yield in this reaction is of the order of MeV which means that no information of the incoming neutron energy can be obtained.

By far the most popular method for detection of fast neutrons is elastic scattering off hydrogen. The reasons for this are that the cross section is quite large and its energy dependence very well known. Also as we shall see, when a neutron is scattered off a proton its entire energy can be transferred to the proton whereas when scattered off a heavier nucleus only a fraction of the neutron energy can be transferred.

2.1 Elastic neutron scattering

In order to understand the elastic neutron scattering, we need to look at the kinematics of the reaction. If A is the mass of the target nucleus (in neutron masses), E_n the kinetic energy of the neutron in the lab system, E_r the kinetic energy of the recoil nucleus in the lab system, θ the scattering angle of the recoil nucleus in the lab system and Θ is the scattering angle of the neutron in the center-of-mass system, cf. Fig. 2.1, then conservation of momentum and energy gives (for non-relativistic energies, $E_n << 939\mathrm{MeV}$)

$$E_r = \frac{2A}{(1+A)^2}(1-\cos\Theta)E_n. \tag{2.1}$$

The transformation to the lab system yields

$$E_r = \frac{4A}{(1+A)^2}\cos^2(\theta)E_n. \tag{2.2}$$

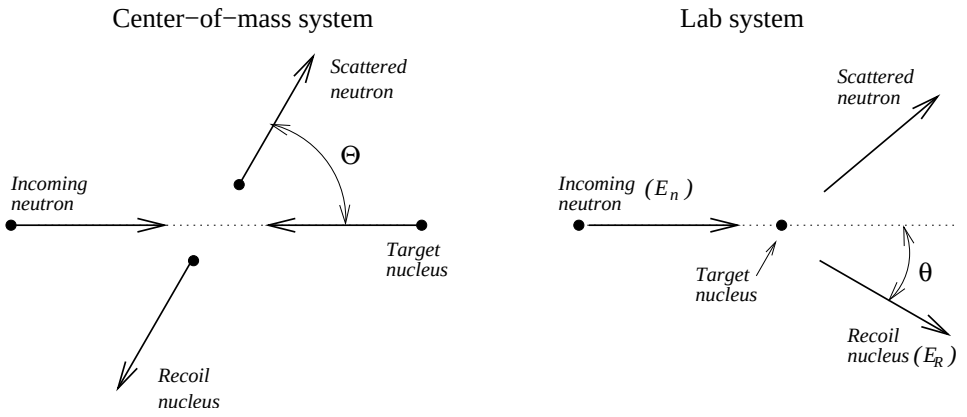

Figure 2.1: Neutron elastic scattering diagram in the center-of-mass and laboratory system.

The maximum energy transferred to the recoil nucleus is thus

$$E_{r_{max}} = \frac{4A}{(1+A)^2} E_n. \tag{2.3}$$

We see that it is only for hydrogen (^{1}H) that the entire neutron energy can be transferred to the recoil nucleus in a single scattering event, and as the nucleus get heavier the fraction of the incoming neutron energy that can be transferred is lower and thus decreasing its importance as a reaction channel. For example, for ^{12}C, the maximum fraction is $\frac{48}{109} = 0.284$.

We must of course also look at the distribution of recoil nuclei, and if we define $\sigma(\Theta)$ as the differential scattering cross section in the center-of-mass system and $P(\Theta)d\Theta$ as the probability that a neutron will be scattered into $d\Theta$ about Θ, then, by definition;

$$P(\Theta)d\Theta = 2\pi \sin\Theta \frac{\sigma(\Theta)}{\sigma_s} d\Theta \tag{2.4}$$

where σ_s is the total scattering cross section integrated over all angles. If we instead look at the probability of having a recoil nucleus with energy E_r we get, since $P(E_r)dE_r = P(\Theta)d\Theta$ and using Eq. 2.1;

$$P(T_r) = \frac{(1+A)^2}{A} \frac{\sigma(\Theta)}{\sigma_s} \frac{\pi}{E_n} \tag{2.5}$$

Hopkins and Breit [Hop 71] have shown that for hydrogen, the differential scattering cross section in the center-of-mass system is nearly isotropic, i.e. $\sigma(\Theta) = \frac{\sigma_s}{4\pi}$. Thus the expected proton recoil energy distribution from a monoenergetic neutron source is a simple rectangle as shown in Fig. 2.1.

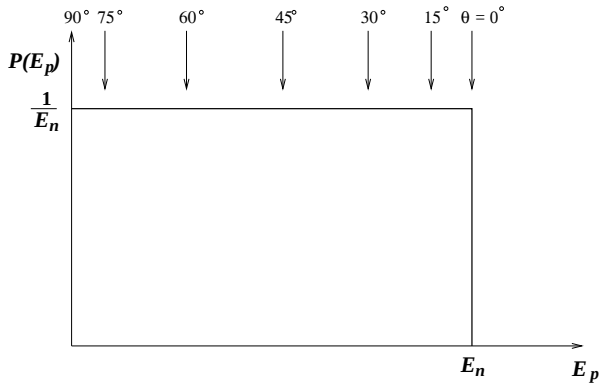

Figure 2.2: Energy distribution of recoil protons from a monoenergetic neutronsource.

For heavier nuclei the situation is not as favourable as for protons, but the effect of the lower fraction of transferred energy and the lower scintillation efficiency (see chapter 3) for these nuclei often means that they do not greatly effect the distribution in Fig. 2.1. Thus, to a first approximation the response function of a detector based on simple hydrogen scattering is assumed to be given by the rectangularly shaped distribution in Fig. 2.1.

2.2 Response Function

As seen above, hydrogen seems to have the best features for being used as a target in elastic neutron scattering detectors and almost all (exception ZnS) scintillators used in fast neutron detectors are thus based on some sort of hydrocarbon molecules, which the upcoming discussion assumes, and when looking at effects distorting the simple rectangular spectrum one must thus be aware of the presence of the carbon.

2.2.1 Light Output vs. Energy

For electrons, the relation between light output and deposited energy is linear (except for energies below ∼125 keV) but for protons the light output, H, is proportional to $\sim E^{3/2}$ where E is the, by the proton, deposited energy (for heavier nuclei the light ouput is proportional to even higher powers of E) [Kno 89]. Thus for protons $H = kE^{3/2}$ and the pulse height distribution is

$$\frac{dN}{dH} = \frac{dN/dE}{dH/dE} = \frac{const}{\frac{3}{2}kE^{1/2}} = k'H^{-1/3}, \tag{2.6}$$

see Fig. 2.3.

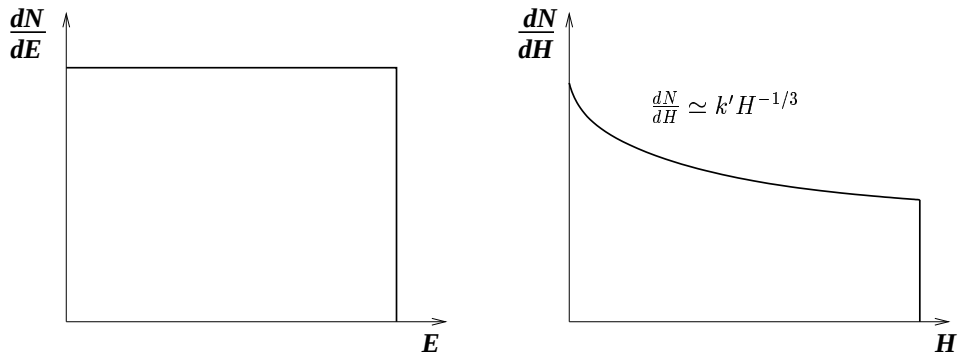

Figure 2.3: Initial proton distribution and the effect of nonlinear light output response on the pulse height distribution.

2.2.2 Effects of the size of the scintillator

- *Small detector compared to the range of the proton*: Some protons will escape the detector and thus deposit less energy than expected and the effect on the response function will be to shift events from high pulse heights to low pulse heights, thus increasing the slope in Fig. 2.3.

- *Large detector compared to the mean free path of the neutrons*: If the detector is large, the chance of multiple scattering off hydrogen becomes non-negligible and since all such events normally occur within a very short period of time compared to scintillation decay processes, the scintillation light from all recoil protons is summed up and a pulse is produced whose amplitude is proportional to the total light output. This effect will thus remove lower pulse height events and add higher pulse height events.

2.2.3 Effects of Carbon

As mentioned before, the carbon does not directly effect the spectra (due to low scintillation efficiency and the fact that only a maximum 28 % of the incident neutron energy can be transferred to the carbon nucleus). The effect on the response function from the carbon is due to the fact that a neutron can undergo a carbon scattering process before scattered off a proton (this effect increases with increased detector size) and the effect on the response function is seen in Fig. 2.4.

If the neutron energy exceeds ∼8-9MeV, the effect of two competing reactions must be taken into consideration:

- ^{12}C(n,α)^{9}Be with threshold 6.17 MeV

- ^{12}C(n,n′)3α with threshold 7.98 MeV

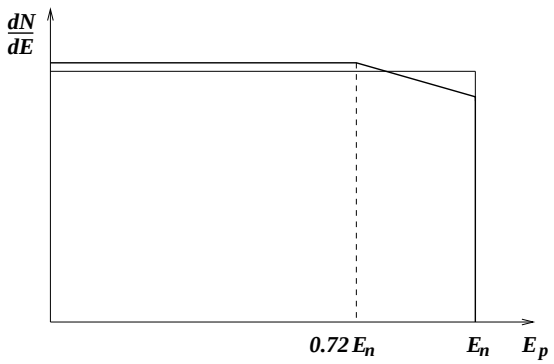

Figure 2.4: The effect on the proton recoil spectrum from carbonscattering.

Note that the scintillation efficiency of the α particles is less than that of protons.

If we look at the total cross section for carbon, see Fig. 2.5, one could ask whether or not the response function should be smooth, but once again we rely on the lower scintillation efficiency of the carbon nucleus: the pulses produced are not large enough, even when multiple scattering is taken into account. This is of course threshold dependent but according to Drosg [Dro 72] a threshold of 500 keV is sufficient to remove the direct effect of the carbon.

2.2.4 Detector resolution

The effect of finite resolution in the detector (due mainly to poor photoelectron statistics) is that the "sharp" features of the response function will be smeared out and the total response function thus obtained is shown in Fig. 2.6.

2.3 Time-Of-Flight

As can be seen above, deriving a response function is everything but trivial. Even if we had an accurate response function, we would still have to use some unfolding techniques on our primary pulse height spectrum in order to obtain the required incident neutron spectrum. Also, the obtained spectrum is an *average* spectrum and no information about the energy of a *single* neutron can be given, thus no so called event-by-event analysis can be done. The need for another method to obtain the neutron energy spectrum is obvious, and nowadays the most used method in fast neutron spectroscopy is the time-of-flight (TOF) method. It relies on fast and accurate time measurements and as such electronics, to complete this task are readily available, the TOF method's popularity is easily understood.

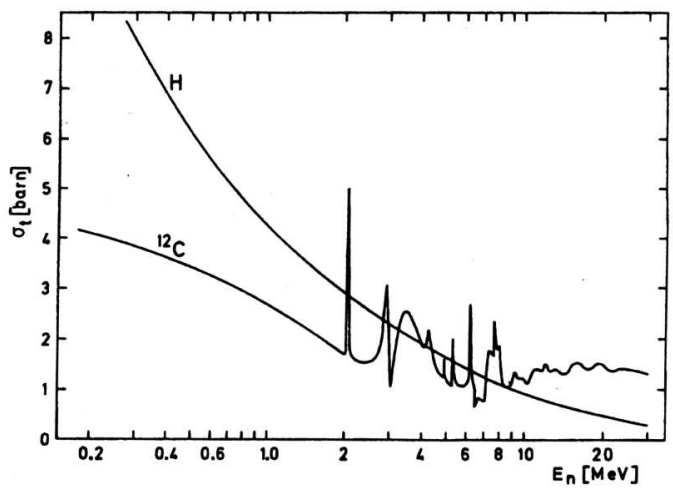

Figure 2.5: Total cross section of hydrogen and carbon as a function of energy. From [Fin 74].

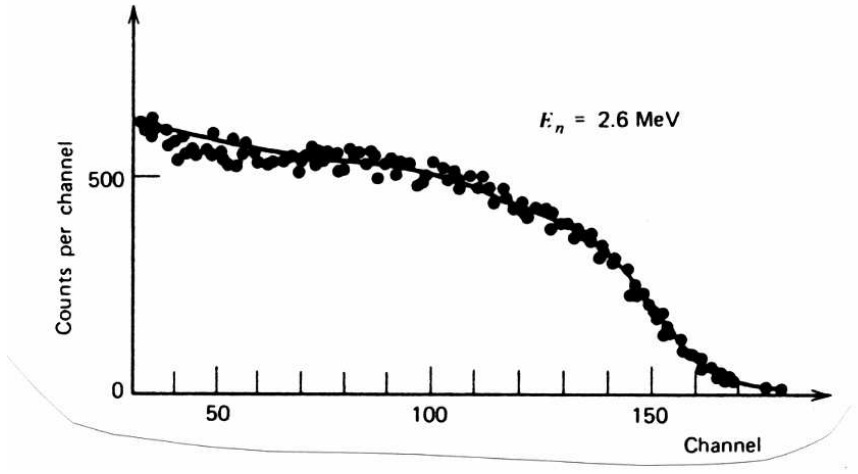

Figure 2.6: Measured pulseheight distribution of a 2.54x2.54 cm cylindric stilbene crystal when irradiated with 2.6 MeV neutrons. From [Kno 89].

The idea behind the TOF method is simple: if one knows the time-of-flight (tof [s]) for a neutron as it transverses a given flight path (fp [m]), then the energy E_n of the neutron is given by

$$E_n = E_0(\frac{1}{\sqrt{(1-\beta^2)}} - 1) \tag{2.7}$$

where

$\beta = \frac{fp}{tof}\frac{1}{c}$
E_0 = neutron rest mass (939.5656 MeV)
and
$c = 2.99792 \cdot 10^8$ m/s.

In order to measure the tof, one basically needs a start pulse, a stop pulse and a TDC (Time to Digital Converter). In our experiment, the start pulse is given by the fission fragment detector and the stop pulse from the neutron detector, (for more information see chapter 5). The energy resolution will be a function of the timing characteristics of the electronics and of the flight path. The longer the flight path the better the resolution (though, at the expense of the solid angle and therefore the count rate).

When low energy neutrons are to be detected there is one important disadvantage with the TOF method one must not forget. It is due to the fact that there, depending on the energy of the neutron, can be a significant difference in speed between neutrons and light. For example, a 5 MeV neutron has speed 31 mm/ns whereas the speed of light in NE-213 is 200 mm/ns. In a 10 cm thick detector (as our detector) the time taken for a 5 MeV neutron and a photon to transverse the detector is 3.2 ns and 0.5 ns respectively. Thus the difference in tof between a 5 MeV neutron, interacting at the front face of the detector and a neutron interacting at the far end (next to the PM[1]-tube) is 2.7 ns. Thus for a thick detector, different tof will be given to neutrons, with the same energy, depending upon where in the detector the scattering occurs.

2.4 Detection Efficiency

As the purpose of this work is to experimentally determine the absolute efficiency of a NE-213 liquid scintillator a few remarks on the efficiency will be given here. Assuming narrow beam geometry and neglecting the

[1]PhotoMultiplier.

effects of the carbon molecules, the intrinsic efficiency can be stated as

$$\epsilon = 1 - e^{-n_H \sigma_{H_s} d} \tag{2.8}$$

where n_H is the number density of hydrogen atoms
σ_{H_s} is the scattering cross section for hydrogen and
d is the thickness of the detector,
i.e. ϵ is the proportion of the incident neutrons that have scattered. If we take the carbon molcules into account, two corrections to Eq. 2.8 have to be made:

1. Neglecting multiple scattering, a scattering off carbon will reduce the neutron flux in the detector, thus the exponent $n_H \sigma_{H_s} d$ will be replaced with $(n_H \sigma_{H_s} + n_C \sigma_{C_s})d$.

2. The neutrons that undergo scattering off carbon do not contribute to the light output due to the difference in scintillation efficiency, thus only the "hydrogen fraction" of the recoil nucleui will contribute to the efficiency:

$$\epsilon = \frac{n_H \sigma_{H_s}}{n_H \sigma_{H_s} + n_C \sigma_{C_s}} (1 - e^{-(n_H \sigma_{H_s} + n_C \sigma_{C_s})d}) \tag{2.9}$$

As we shall see, the value of the pulse height threshold set on the system greatly effects the efficiency. If B is the threshold used, then (assuming the rectangular shaped proton recoil distribution in figure 2.1) only the fraction $(1 - \frac{B}{E_n})$ of the scattered recoil protons will produce pulses higher than the threshold. Thus to a first approximation, the efficiency is;

$$\epsilon(B, E_n) = (1 - \frac{B}{E_n}) \frac{n_H \sigma_{H_s}}{n_H \sigma_{H_s} + n_C \sigma_{C_s}} (1 - e^{-(n_H \sigma_{H_s} + n_C \sigma_{C_s})d}) \tag{2.10}$$

According to Schwarz and Zetterström [Sch 66], Eq. 2.10 works quite well for neutron energies up to ∼8 MeV.

The standard procedure to determine the efficiency is to use Monte Carlo calculations. The computer code developed by Stanton [Sta 71] and improved by McNaughton et al. [Mcn 75] and Cecil et al. [Cec 79], is widely used. In this code the following reaction channels are taken into account:

- np elastic scattering
- n^{12}C non-diffractive elastic scattering
- ^{12}C(n,n$'\gamma$)^{12}C
- ^{12}C(n,α)^{9}Be
- ^{12}C(n,n$'$)3α

- ^{12}C(n,np)^{11}B and ^{12}C(n,2n)^{11}C or ^{12}C(n,p)^{12}B and ^{12}C(n,2n)^{11}C
- n^{12}C diffractive elastic scattering

The input parameters in the code are the geometry and the relative light response function[Cec 79];

$$T_e = a_1 T_p - a_2(1 - e^{-a_3 T_p^{a_4}}) \tag{2.11}$$

where T_p [MeV] is the energy of the proton and T_e [MeV] is the equivalent electron energy. The a_i factors are material dependent parameters and for NE-213 they are 0.83, 2.82, 0.25 and 0.93 respectively. Equation 2.11 is also applicable to α-particles, then with parameters 0.41, 5.9, 0.065 and 1.01 respectively, (and is valid for all hydrocarbon scintillarors).

2.4.1 Measuring the efficiency

The Monte Carlo detector efficiency calculations must be justified by experimental results and several attempts have been made to measure this efficiency, [Ver 68], [Ede 72], [Dro 72], [Fow 80] and [Gul 89]. When speaking of efficiency measurements, one has to be reminded that each detector and experimental setup is unique and the efficiency may vary due to differences in impurities, different decay constants, different drifts in PM tubes etc.. However, the detectors and PM tubes have been manufactured with great accuracy to minimize such differences. Nevertheless, mainly two methods have been applied to experimentally determine the efficiency:

1. *Comparison with a calibrated detector.*
2. *Associated particle method.* Measuring, the flux of neutrons that impinge upon the detector, by detecting the associated charged particle(s) of the neutron producing reaction. Possible reactions are; T(p,n)^{3}He, T(d,n)^{4}He, H(n,n)p or, as in our experiment, spontaneous fission of ^{252}Cf.

A comparison between Stanton code and measurements can be seen in Fig. 2.7.

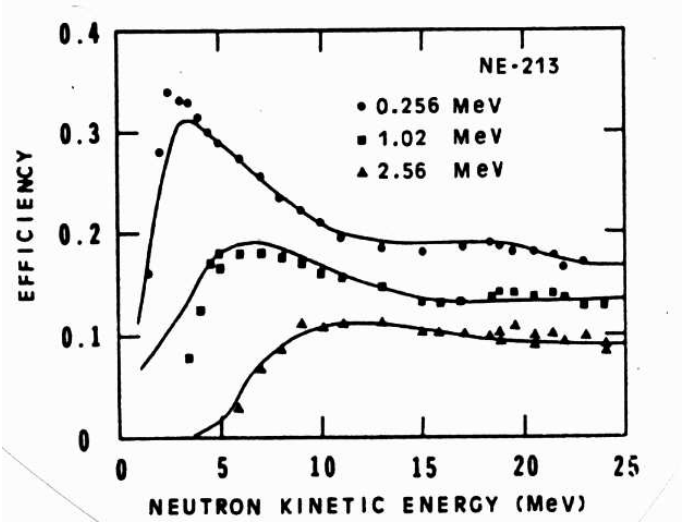

Figure 2.7: Comparison of efficiency measurements (points) with Stanton code calculations (continous lines) for NE-213. From [Cec 79].

Chapter 3

Scintillators

When manufacturing proton recoil scintillators, the choice of some sort of organic scintillator is obvious. The first scintillators used for neutron spectroscopy were anthracen and stilbene crystals. Anthracen has the highest scintillation efficiency of all organic scintillators and one usually states the scintillation efficiency in percentages of that of anthracen. Stilbene was used when pulse shape discrimination techniques were desired. One great disadvantage of anthracen and stilbene is the anisotropy in scintillation efficiency; the light output is dependent on the charged particles direction relative to the crystal axis. This will, of course, spoil the energy resolution. Also anthracen and stilbene are difficult and thus expensive to manufacture in large sizes.

Nowadays, proton recoil scintillators in a liquid or a solid form are both cheap and easy to manufacture in different shapes and sizes. The liquid scintillator basically consists of an organic scintillator dissolved in an appropiate solvent. Often, activators and wavelength shifters are added.

3.1 Scintillation mechanism in organic scintillators

In order to understand the important pulse shape discrimination property of some of the scintillators, we have to look at the scintillation mechanism. Unlike inorganic crystalline scintillators, like NaI(Tl), the scintillation process in an organic scintillator arises from transitions in a single molecule independent of its physical state. Many of the practical organic scintillators are based on molecules with certain symmetry properties which give rise to what is known as π-electron structure. The energy levels of such a structure are shown in Fig. 3.1.

The main features in the structure are the singlet (S_x) and triplet (T_x) states and each of these levels are furthermore subdivided into vibrational states (S_{xy}) and (T_{xy}). The spacing between S_0 and S_1 is 3-4 eV and the spacing between the vibrational states is $\sim$0.15. eV.

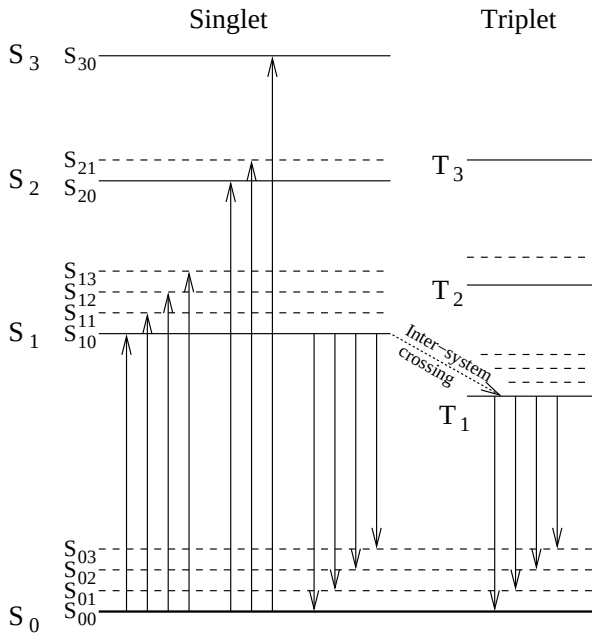

Figure 3.1: Energy levels of an organic molecule with π-electron structure. From [Bir 64].

Since, at room temperature, $kT = 0.025$ eV[1], all molecules at room temperature are in the S_{00} state. When a charged particle passes by, the molecule can absorb energy which is represented by the absorption arrows. Excitation to higher singlet states (S_2, S_3 etc.) are quickly deexcited through radiationless internal conversion to the S_1 state and molecules excited to levels with excess vibrational energy (S_{11}, S_{12} etc.) quickly lose that vibrational energy due to the lack of thermal equilibrium. Thus, the net effect of the excitation after a short time ($\sim$ps) is to have a population of excited molecules in the S_{10} state. From this S_{10} state, there are basically three different routes:

1. *Transition to one of the vibrational states of the ground state.* This is known as prompt fluorescence and constitutes the principle scintillation light. It is a relatively fast process with decay times of the order of ns. Note also that all transitions (with the S_{10}-S_{00} as an exception) will have longer wavelengths than needed for absorption of the same molecule, thus transparency.

2. *Transition to the triplet state T_1 through intersystem crossing.* The lifetime of T_1 ($\sim$ms) is characteristically much longer than that of S_{10}, so the radiation emitted[2] in the deexcitation to S_0 do

[1] kT is Boltzman's constant times the temperature.
[2] This radiation is denominated phosphorescence.

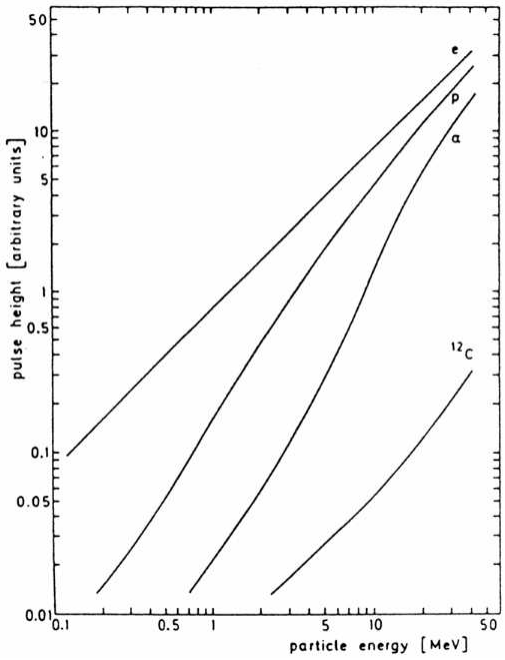

Figure 3.2: Relative response of NE-213 to electrons, protons, α-particles and carbon ions. From [Ver 68].

not contribute to the pulse produced by the prompt fluorescence. However, instead of a transition to S_0, some of the molecules can be excited back to S_{10} and then decay to S_0 through what is called delayed fluorescence. It is the delayed fluorescence that constitutes the slow part of the scintillation light.

3. Unfortunately, there are modes of deexcitation which are radiationless, the excitation energy is instead degraded mainly to heat. All such radiationless deexcitations are grouped under the term quenching. The difference in scintillation efficiency (defined as the fraction of all incident particle energy which is converted into visible light) between different types of radiation (cf. Fig. 3.2) is due mainly to the different amount of quenching. A high ionization density is believed to lead to quenching from damaged molecules along the track and thus lower scintillation efficiency.

Of course the picture given above of the scintillation mechanism is a simplification and the actual case is much more complicated. The excitation energy usually undergoes transfer from molecule to molecule before deexcitation which makes it possible to add molecules with e.g. high scintillation efficiency in which the deexcitation finally occurs. Sometimes, also so called waveshifter are added, which can make the

scintillator more transparent or make the emitted light better match the properties of the photocathode.

3.1.1 Pulse Shape Discrimination

We now move our attention to the pulse shape. As said in the preceding section, the principle scintillation light is represented by the prompt fluorescence characterized by a decay time of the order of ns. Besides this fast component, there are also a slow component corresponding to the delayed fluorescence which has a decay time of the order of 100 ns.

The pulse shape discrimination techniques uses the fact that the fraction of the light that appears in the slow component depends on which kind of particle causes the ionization. The nature behind this effect is as follows: the slow component arises because of excitation from T_1 to S_1 and the subsequent fluorescence. But two T_1-molecules can interact with each other and form a product molecule in which one of the molecules will be in the S_1 state and the other in the ground state, thus, this bimolecular reaction will increase the slow component light output, and the rate at which these bimolecular reactions occur depends on the square of the concentration of T_1-molecules. Higher ionization density will thus lead to higher fraction of slow component light.

When a neutron interacts in a scintillator it produces protons while a γ produces elctrons. This difference in reaction products makes it possible to discriminate between neutrons and γ:s. Fig. 3.3 shows some different pulse shapes in stilbene.

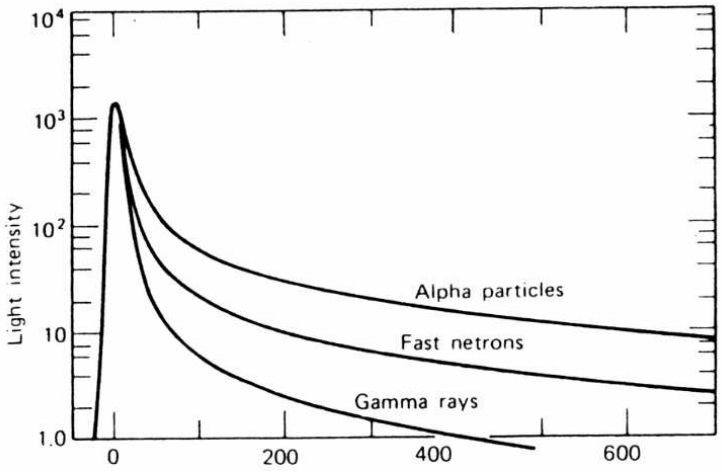

Figure 3.3: The time dependence of scintillation pulses in stilbene when excited by radiations of different types.

A problem one encounters with liquid scintillators is the effect of dissolved oxygen which not only decreases the scintillation efficiency due to the alternative ways of radiationless deexcitations it provides, but also hinders the slow component of the light more than the fast which thus obstruct pulse shape discrimination. If a liquid scintillator is to be used in an experiment in which pulse shape discrimination will be employed, it should, prior to use, be deoxygenated by bubbling the liquid with either nitrogen gas or some inert gas.

3.1.2 NE-213

The most used scintillator for neutron spectroscopy is the liquid scintillator NE-213 manufactured by Nuclear Enterprises Limited [Nuc Ent]. Its popularity is mainly due to its excellent pulse shape discrimination properties, comparable with that of stilbene. It is usually encapsulated in an aluminium or glass container, which, of course, makes it easy for the manufacturer to comply with many different requests regarding size and shape.

The scintillator, which must be considered as cheap, consists of purified xylene, naphtalene, activators and waveshifter. Some technical data on NE-213 can be seen in Table 3.1.

Table 3.1: Some technical data on NE-213. From [Nuc Ent].

Density	0.874 g/cm^2
Refractive Index	1.508
Light Output (% Anthracen)	78
Decay Time (fast)	3.7 ns
Wavelength of maximum emission	425 nm
Ratio of H to C atoms	1.213

Chapter 4

The Source: Californium-252

A key role in the experiment is played by the source, californium-252, and in order to fully comprehend this experiment some facts must be known about it. Also, being a material undergoing spontaneous fission, it is, of course, interesting in itself. A general reference on fission can be found in [Hui 73], an early but good reference on ^{252}Cf is [Bow 62], a later and very thorough one is [IAEA 86].

4.1 Fission

In order to get a quick and easily understandable picture of nuclear fission, one can look at the binding energy per nucleon, see Fig. 4.1.

For example, $^{238}_{92}$U has a binding energy of about 7.6 MeV per nucleon while a nuclei with A =119 (= $\frac{238}{2}$) has a binding energy of about 8.5 MeV per nucleon. Thus the fissioning of $^{238}_{92}$U, with a total binding energy of 1809 MeV, into two $^{119}_{46}$Pd fragments with a total binding energy 2023 MeV, releases 214 MeV, of which some 80 % appears as kinetic energy of the two fragments. The rest of the energy appears as γ, n and β emission from the fragments. Note that the example given above is deceptive, it is much more probable for a nucleus to fission into two fragments with different mass[1].

Fission has to be considered as a very efficient way of decreasing the energy of a nucleus energy but it also has to be considered as a very rare process (as compared to other decay processes). For example the half life of ^{238}U is $4.5{\cdot}10^9$ y, while the partial half life for fission is $\sim 10^{16}$ y. It is not until mass numbers greater than 250 that fission plays an important role as a decay process.

In analogy with the α-decay process, the Coulomb barrier inhibits the fission process. Fig. 4.2 is of course a great oversimplification but as an illustration it serves its purposes well. In the case of spontaneous fis-

[1]For ^{238}U, the most probable division is into two fragments with mass numbers $\approx$96 and $\approx$142.

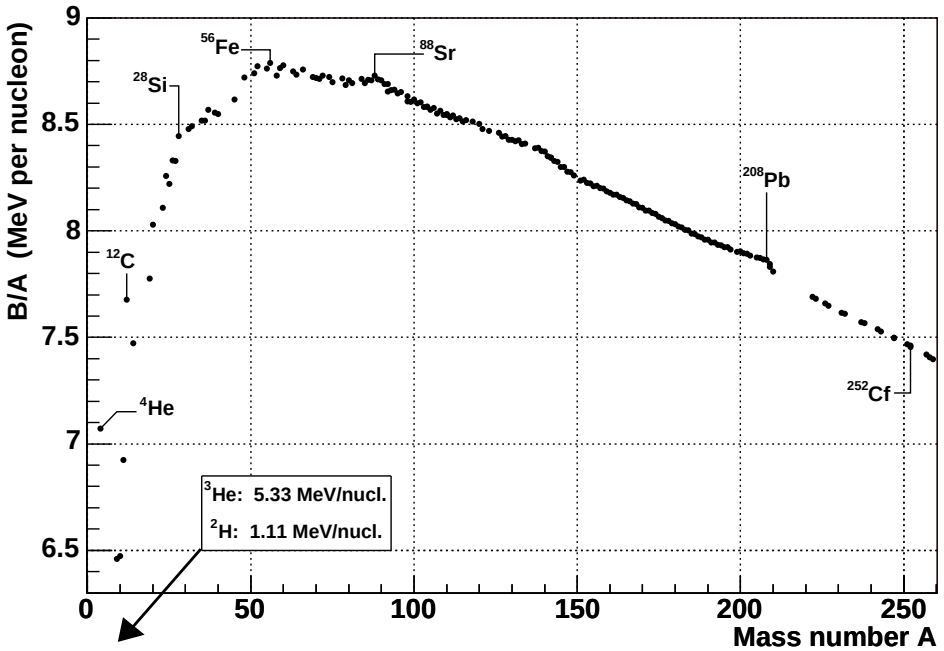

Figure 4.1: Binding energy per nucleon as a function of mass number.

sion, the probability of barrier penetration (tunneling) is non-negligible while in the case of induced fission, an absorption of e.g. a neutron will put the nucleus above the barrier and a prompt fission will occur.

4.2 Gammas from fission

Since the γ:s emitted in the fission process make it possible to put the TDC time scale in a TOF experiment on an absolute basis some brief information about γ:s will be given here. In a ^{252}Cf fission event, the average number of prompt γ:s emitted is approximately 10. This is the *total* number of γ:s and if we only look at γ:s with energies higher than 1 MeV the γ multiplicty has decreased to about 2 [Bru 82].

In regard to the current work, the interesting fact about the γ:s are on which time scale they are emitted and it is believed that more than half the γ:s emitted in a typical fission event have half lifes shorter than $2{\cdot}10^{-11}$ s. In Fig. 4.3, the fraction of γ yield as a function of time is given. This function is assumed to apply to both the fission of ^{252}Cf and ^{235}U.

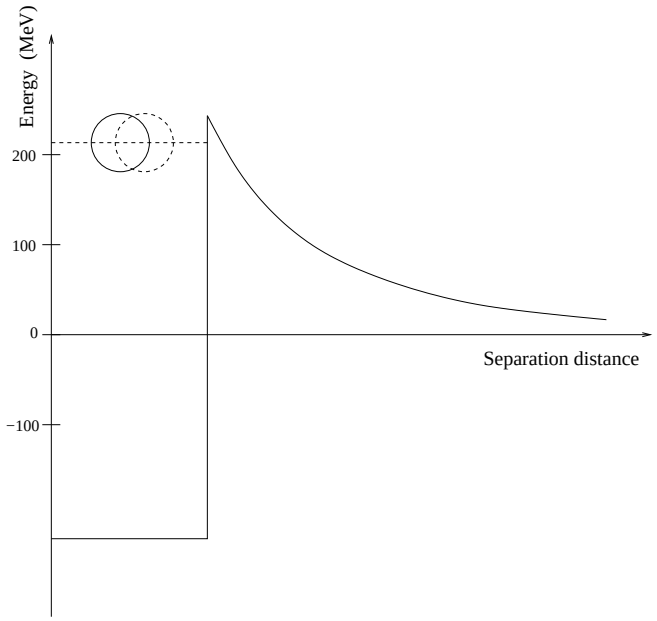

Figure 4.2: Very simplified picture of the nuclear potential well. The two fragments that perhaps exist in the well are prevented to fissionate by the Coulomb barrier.

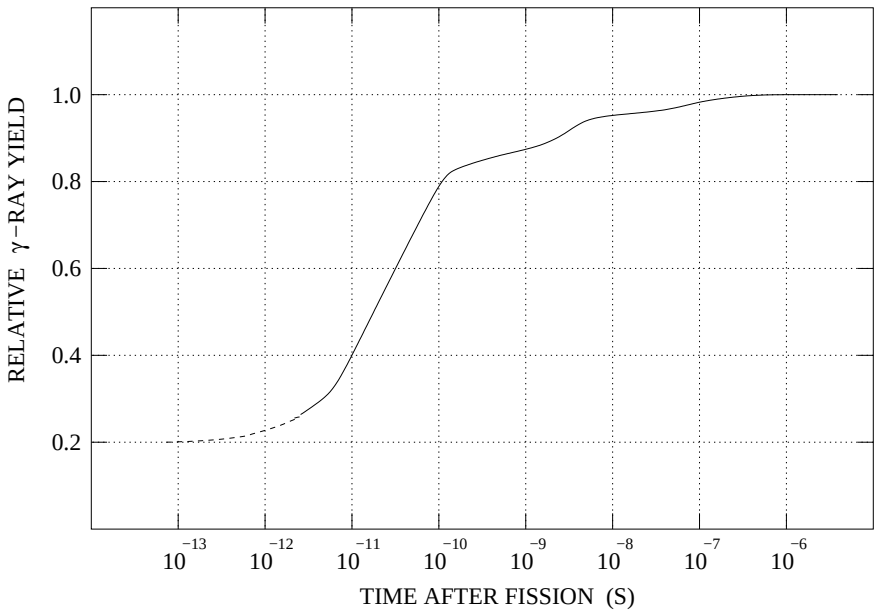

Figure 4.3: Fraction of γ yield as a function of time, for ^{252}Cf and ^{235}U. From [Hui 73].

4.3 Neutrons from fission

Most of the ∼20 % of the total energy released that appears as β, γ and neutron emission from the fragments are carried away by the neutrons. The emission of neutrons in fission is a complex process with many different parameters and much has been written about it, since a lot of insight into the fission process can be gained by studying the neutrons. We will, however, only deal with the areas of the subject that deal specifically with the current work.

4.3.1 Time Scale

One way of categorizing the neutrons is on which time scale they are emitted. A first division is into prompt and delayed neutrons. The delayed neutrons are emitted following a β-decay of a primary fission fragment and the time scale is thus of the order of seconds after the fission event. The fraction of delayed neutrons to the total number of neutrons is usually very small, e.g. for ^{252}Cf it is 0.002, thus for our purposes they play no significant role.

Even though the term prompt neutrons indicates that the neutrons were emitted promptly after fission, there still is a structure in the "promptness". It is believed that in a typical fission process some 10 % of the neutrons are emitted at scission and thus giving rise to a flat angular distribution. The rest of the neutrons (except for those emitted during the acceleration) are assumed to be emitted by fully accelerated fragments and the neutrons will thus appear in directions strongly correlated with the fragment direction. The fission fragments are assumed to be nearly fully accelerated $\sim 10^{-20}$s after scission and most of the neutrons are emitted at times shorter than $\sim 10^{-14}$s [Fra 52]. Thus, on the ∼ns time scale used in our TOF measurement, all neutrons are assumed to be emitted at time zero.

4.4 Nubar

The term nubar refers to the symbol $\overline{\nu}$ meaning the average number of neutrons emitted in a fission event and is, in our experiment, a very important number. In Fig. 4.4, $\overline{\nu}$ is plotted for some different fission sources. For ^{252}Cf $\overline{\nu}$ =3.766 but this includes a delayed part of 0.009, thus the prompt $\overline{\nu_p}$ for ^{252}Cf is

$$\boxed{\overline{\nu_p} = \mathbf{3.757}}$$

In Table 4.1 the probability mass function[2] of the number of prompt

[2] P_i is the probability that i neutrons are emitted in a fission event.

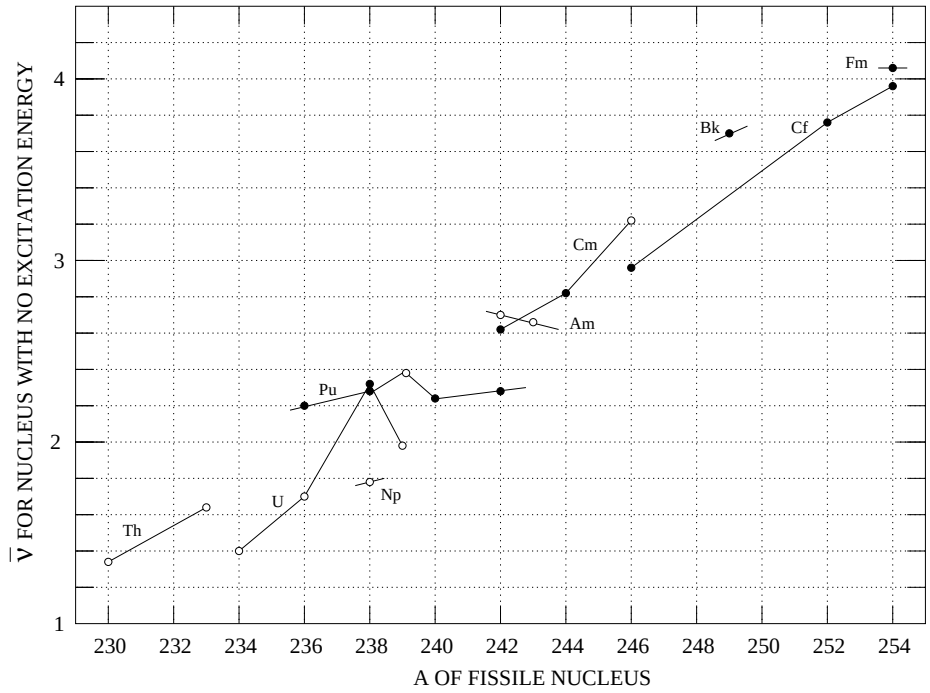

Figure 4.4: $\overline{\nu}$ for some different fission sources

neutrons from ^{252}Cf is given.

Table 4.1: Probability mass function of the number of prompt neutrons from ^{252}Cf. From [Bol 85].

P_0	0.00209±0.00012
P_1	0.02621±0.00037
P_2	0.1262±0.0008
P_3	0.2752±0.0012
P_4	0.3018±0.0015
P_5	0.1846±0.0010
P_6	0.0668±0.0009
P_7	0.0150±0.0005
P_8	0.0021±0.0003
$\overline{\nu_p}$	3.757

4.5 A closer look at ^{252}Cf and its neutron spectra

Californium was the sixth transuranium element to be discovered and was first produced by Glenn Seaborg and collaborators in 1950 in Berkely [Han 75]. The isotope ^{249}Cf is obtained from the β-decay of

^{249}Bk while the heavier isotopes are produced by intense neutron irradiation by the reactions

^{249}Bk(n,γ)^{250}Bk $\stackrel{\beta^-}{\rightarrow}$ ^{250}Cf
^{249}Cf(n,γ)^{250}Cf and
^{250}Cf(n,γ)^{251}Cf(n,γ)^{252}Cf.

From a chemical point of view californium-III is the only californium ion stable in aquos solution, and when handled as a solid it is usually in the form of californiumoxide (Cf_2O_3) or californiumtrichloride ($CfCl_3$).

The great interest given to ^{252}Cf is due to its high (3.09 %) spontaneous fission branch combined with its high specific activity, resulting from the 2.65 y half life and the high neutron yield ($\overline{\nu_p}$ =3.757). All these properties make the nuclide unique for the study of the physics and chemistry of fission, as a source of fission fragments, as a neutron standard and as a neutron source. A trivial fact about ^{252}Cf resulting from its versatile applicability, is that according to Guinnes Book of World Record [Gui 97], californium is the per weight most expensive material in the world ($\sim$ \$ 1000/μg).

We now turn our attention to the neutron spectra of ^{252}Cf. A good starting point for this is Fig. 4.5. In Fig. 4.5, the main features of the neutron spectrum are shown. We see that the neutron density is strongly peaked in the forward directions of the fragments (conservation of momentum makes the fission fragments move 'back to back') and that more neutrons are emitted from the light than the heavy fragment (the two fragments will have approximately the same neutrons to protons ratio as ^{252}Cf, thus giving the lighter fragment a higher neutron excess). Fig. 4.5 also shows that the intensity quickly drops off as the neutron energy increases, the average energy is found to be $\sim$2.13 MeV.

In an experiment by Budtz-Jørgensen *et al.* [Bud 88], the angular distribution, $W(\theta)$ of neutrons in a fragments center-of-mass system was measured and their result was;

$$W(\theta) = 1 + (0.01 \pm 0.02) P_2(\cos\theta) \tag{4.1}$$

where $P_2(\cos\theta)$ is the Legendre polynomial of second power, thus no significant anisotropy to within 2 % accuracy.

4.5.1 Models

Empirically, it is thus well established that practically[3] all fission neutrons are emitted from fully accelerated fragments and the neutron emission is practically isotropic in each fragments rest system. The most simple, macroscopic description of the neutron spectrum is built

[3]With the exception of the scission neutrons

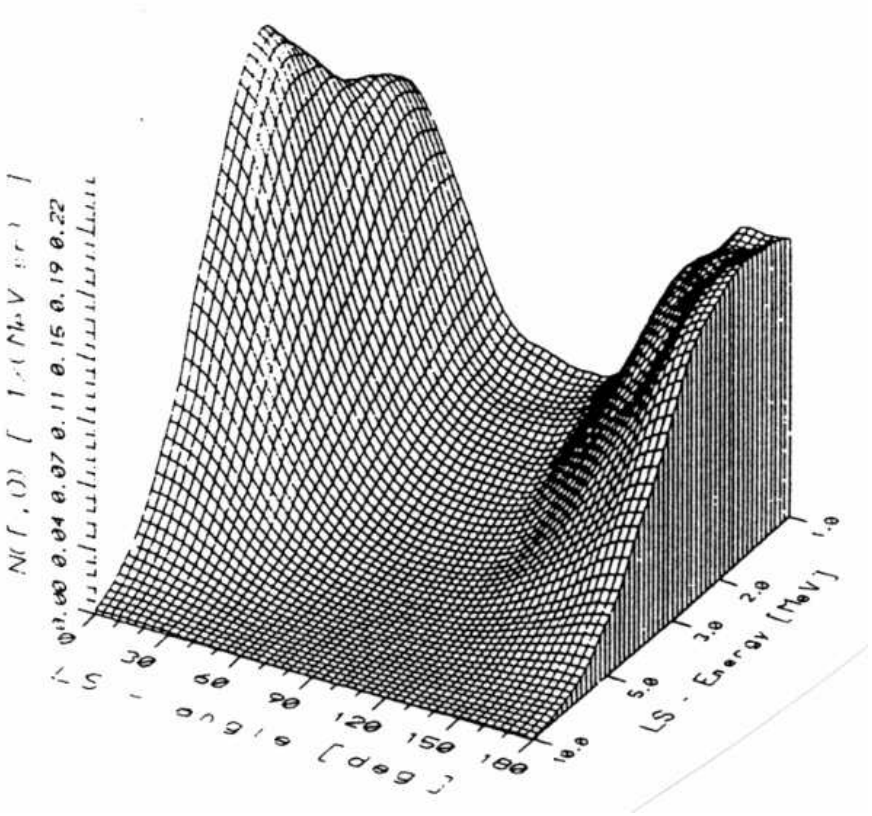

Figure 4.5: Experimentally measured double differential energy and angular distributions of neutrons from ^{252}Cf. The angles are with respect to the light fission fragment and 'LS' refers to lab system. From [Arn 89].

on the assumption that the lowest non-vanishing moment of the p'_i (momentum in $i = x, y, z$ direction, the $'$ refers to center-of-mass system) distribution is $< p_i'^2 >$, and that all higher moments are negligible. If the entropy is maximized we get a three dimensional Gaussian momentum distribution which transforms into the well known Maxwell energy spectrum;

$$N_M(E')dE' = \frac{2}{\sqrt{\pi}} \frac{\sqrt{E'}}{T_M^{3/2}} e^{-E'/T_M} dE' \tag{4.2}$$

in which $N_M(E')dE'$ is the fraction of neutrons having energy in the interval $(E, E + dE)$. The spectrum is characterized by the single parameter T_M, called the temperature parameter, and the average energy is;

$$< E' >= \frac{3}{2} T_M \tag{4.3}$$

Eq. 4.2 is valid in the fragment's rest system, thus the primes, but by means of a Galilei transformation we can go to the laboratory

system:

$$\overline{p} = \overline{p'} + \overline{q} \tag{4.4}$$

where $\overline{q}$ is the fragments momentum per nucleon. The distribution thus obtained is a Watt spectrum which has the form;

$$N_W(E)dE = e^{-E_W/T_W} \frac{\sinh(\sqrt{4EE_W/T_W^2})}{\sqrt{4EE_W/T_W^2}} N_M(E)dE \tag{4.5}$$

As can be seen in Eq. 4.5 the Watt spectrum is characterized by the two parameters T_W and E_W and the average energy is;

$$< E >= \frac{3}{2}T_W + E_W \tag{4.6}$$

To complete the spectrum in the laboratory system, one should average the Watt spectra over all possible values of T_W and E_W for the various fission fragments, but it turns out that the superposition of two Watt spectra hardly differs from a single Watt distribution. Therefore we may expect that a single Watt spectrum with effective parameters T_W and E_W will give a reasonable description of the true neutron spectra. A measurement made by Fröner [Frö 90] shows that with Watt parameters T_W=1.18 MeV and E_W=0.36 MeV, a good fit to the experimental lab neutron spectra can be achieved, see Fig. 4.6. However, if we compare the Watt spectra above with a Maxwellian spectra with temperature parameter T_M=1.42 MeV we see, in Fig. 4.7, that there is not much difference between them.

Since the Watt spectra is not without discrepancy when compared to more accurate measurements, the standard lab neutron emission spectra from ^{252}Cf is (according to IAEA recommendations, [IAEA 86]) a *Maxwellian with T_M=1.42 MeV together with a correction function.* Fig. 4.8 and Fig. 4.9 show the correction function (in terms of four straight lines[4]) and the corrected Maxwellian energy distribution used in this experiment.

Microscopic Models

The existence of a correction function above does, of course, imply that the assumptions that led to the Maxwellian and Watt spectra are inadequate. The theoretical analysis of neutron emission from diverse fragments should start with a definition of a probability distribution for the fission fragments

$$P(A, Z, E^*, TKE, J, ...) \tag{4.7}$$

[4] A more accurate correction function in terms of a spline function is available but for our purposes four straight lines will be more than sufficient.

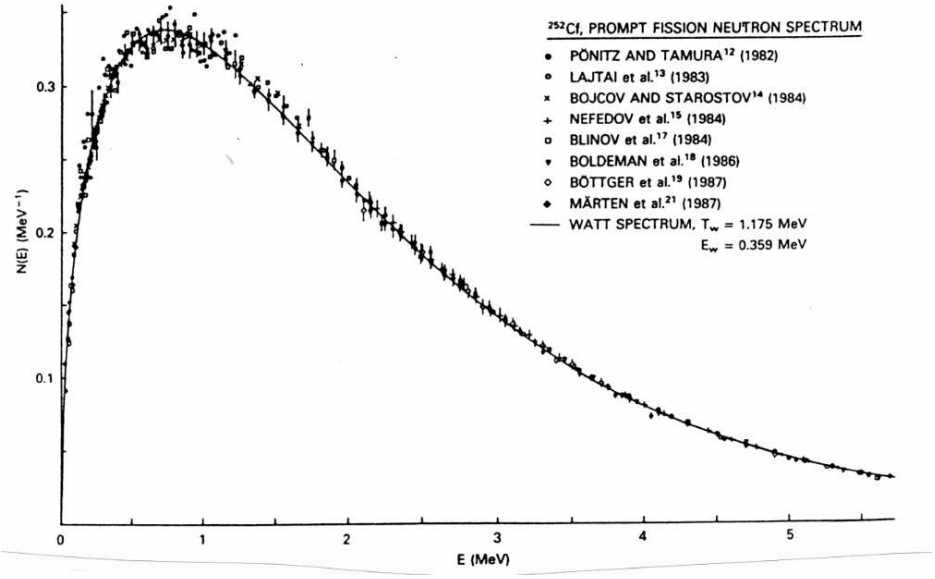

Figure 4.6: Watt spectra with parameters T_W=1.18 MeV and E_W=0.36 MeV and experimental data (most error bars omitted for clarity). From [Frö 90].

in nucleon numbers A and Z, excitation energy E^*, total kinetic energy TKE, angular momentum J, ... , and then describe the probability of neutron emission for each individual fission fragment. This is a problem with tremendous complexity and far beyond the scope of this project. We will only give a reference [Mär 90] in which further references are given to some of the different models that so far have been worked out. We will also mention that, as far as we know, no model is yet able to give accurate predictions over the entire energy range covered by the neutrons (0.2-20 MeV).

4.5.2 Angular Distribution

In order to avoid any confusion, let it first be noted that the Maxwell energy spectrum in the above section is a *non-coincidence* spectrum, whereas the spectra refering to angular distributions are *coincidence* spectra, but a coincidence spectrum *without* angular dependence will show a corrected Maxwellian energy dependence as in Fig. 4.9.

With reference to Fig. 4.5, we infer that if a light fission fragment is detected (and thus defining a z-axis) there will be a neutron distribution in energy and space, $\rho_L(E, \theta, \varphi)$. Note that in Fig. 4.5 the φ angle has been integrated, and thus θ is the lab system angle in Fig. 4.5. However, in our experiment, we do not discriminate between the light and heavy

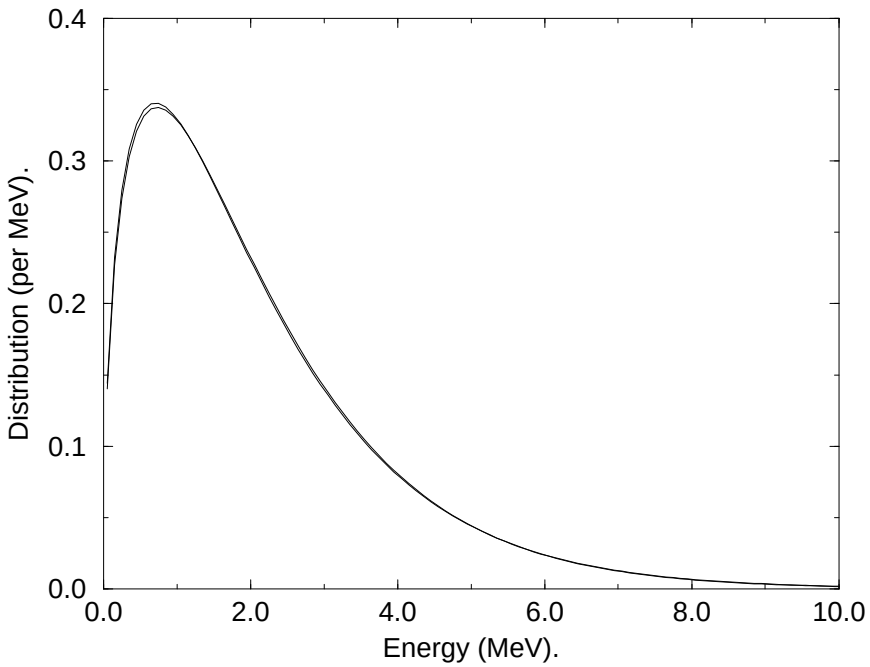

Figure 4.7: Maxwellian and Watt distributions according to Eq. 4.2 and Eq. 4.5, having parameters T_M=1.42 MeV and T_W=1.18 MeV and E_W=0.36 MeV.

fragments. Assuming an equal probability of detection, we therefore introduce the average neutron distribution, $\rho(E,\theta,\varphi) = \frac{1}{2}(\rho_L + \rho_H)$, which thus is symmetric with respect to θ=90°, and the normalization of this distribution reads;

$$\int_{E=0}^{\infty}\int_{\theta=0}^{\pi}\int_{\varphi=0}^{2\pi}\rho(E,\theta,\varphi)d\Omega dE = \overline{\nu} \tag{4.8}$$

If a neutron detector, subtending a solid angle of $\Delta\Omega_n$, was to be placed in a direction (θ_n,φ_n), the number of neutrons, $N(E,\theta_n,\varphi_n)$, hitting the detector per detected fission fragment would be

$$N(E,\theta_n,\varphi_n) = \int\int_{\Omega_n}\rho(E,\theta,\varphi)d\Omega \approx \rho(E,\theta_n,\varphi_n)\Delta\Omega_n \tag{4.9}$$

assuming a constant distribution function over $\Delta\Omega_n$ ($\approx$ 5.4 msr).

In our experiment, the fission detector subtends a large solid angle $\Delta\Omega_f$ ($\approx$ 0.5 sr), thus in order to get the number of neutrons hitting the neutron detector when a fragment is detected in the fission detector, we must average over the angles subtended by the fission detector. Because of the large solid angle $\Delta\Omega_f$, the source can not be considered a point source, and the geometry of the problem is not very well defined.

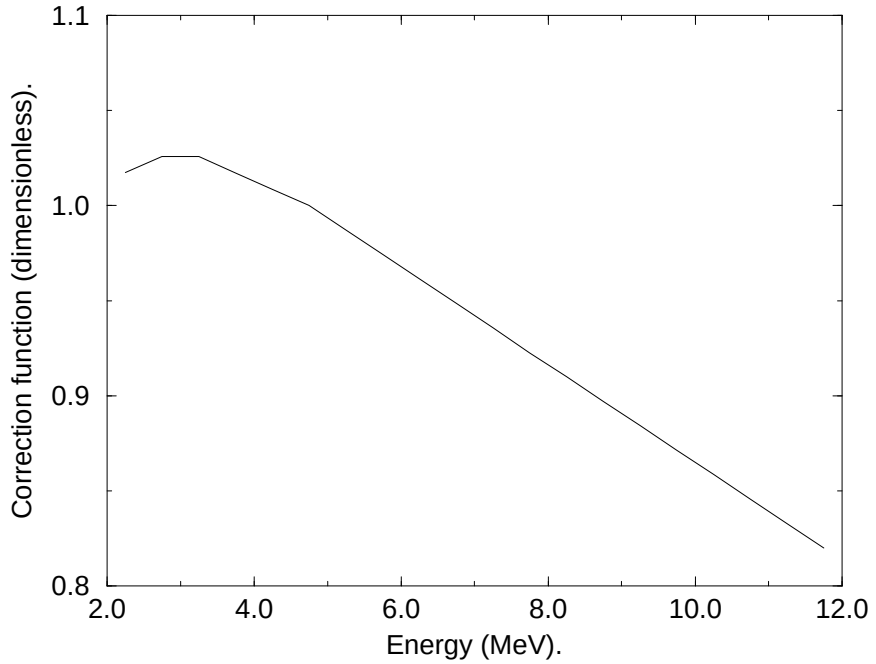

Figure 4.8: The correction function that is to be multiplied to the Maxwellian spectra with T_M=1.42 MeV in order to get the, so far, most accurate 'theoretic' neutron emission spectra.

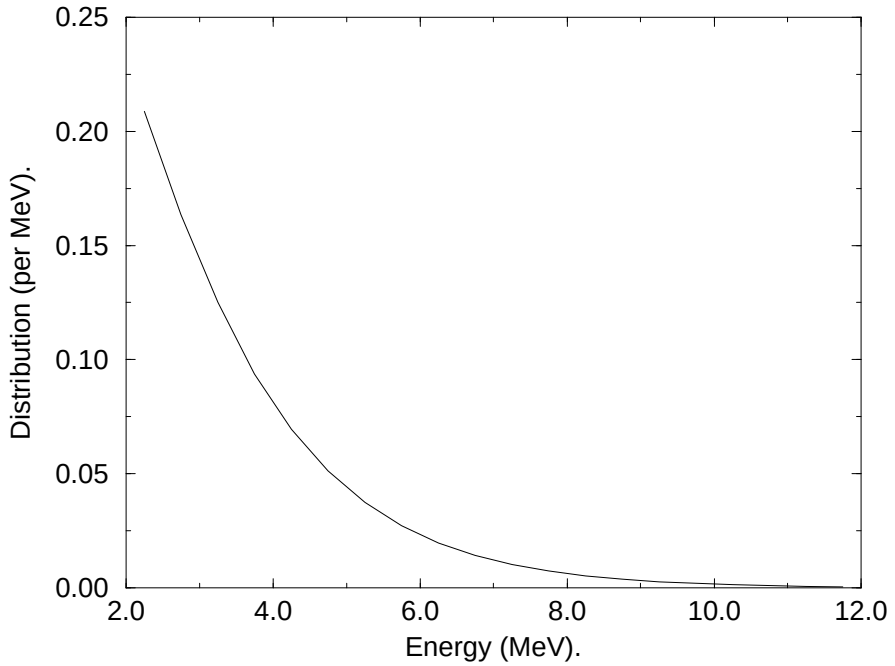

Figure 4.9: The corrected Maxwellian spectra used in this experiment.

The difficulties in using a theoretical[5] angular distribution $\rho(E, \theta, \varphi)$ in obtaining an expected distribution leads us to deal with the problem in a more pragmatic way. Thus, as is customery in angular correlation experiments, the measured angular distribution, $W(\Theta)$, is fitted to a series of even[6] powers of Legendre polynomials;

$$W(\Theta) = const(1 + K_2 P_2(\cos\Theta) + K_4 P_4(\cos\Theta) + ...) \qquad (4.10)$$

In Eq. 4.10, we note that all angular dependency is within the parenthesis and if no angular dependency was present, we would have measured *const* coincidences for all angles Θ. Since $P_l(\cos(0))$=1 for all $l > 1$, the factor $GEO \equiv (1 + K_2 + K_4 + ...)$ [7] is a measure of how many times more coincidences are detected at angle Θ=0° because of the existence of an angular distribution. For further information on the angular distribution and the calculation of the geometrical enhancement factor, see chapter 7.

4.6 Our Source

Our ^{252}Cf source was supplied by Isotopes Products Laboratories and consisted of approximately 370 kBq (as of 31 March 1997) which corresponds to about 0.02 μg and consisted of californiumoxide electrodeposited on a platinium clad nickel foil. The activity is covered with 50 μg/cm^2 gold to prevent loss of ^{252}Cf atoms by recoil. The area of the activity is approximately 0.2 cm^2 which means that the thickness of the source itself is about 0.1 μg/cm^2.

The thickness of the gold layer and the activity layer must of course be seen in the light of the ranges of the fission fragments. A rule of thumb suggested by Knoll [Kno 89] for assessing the range is to use half the range of a 5 MeV α-particle as the range of a typical fission fragment. Using the ranges for protons [Ato 82] and then via scaling to ranges of α-particles one finally obtains the following ranges.

In gold and platinium: $\sim$ 9 mg/cm^2
In nickel: $\sim$ 4 mg/cm^2

We thus see that the gold layer is negligible (consists of only 1 part of 180 of the total range in gold) and even though we do not have any figures on the ranges in californiumoxide (a good approximation would probably be that the ranges do not differ a lot from that of gold and platinium) we can state that due to its very thin thickness, only a negligible amount of the fragments will be absorbed in the source

[5] Theoretical in the sense of 'as described by others'.

[6] If odd powers were to be used, the function would not be symmetric with respect to 90°

[7] GEOmetrical enhancement factor

itself. Regarding the nickel foil backing, which according to the manufacturer is 0.0127 cm thick, (113 mg/cm^2), which means that no fission fragments can penetrate this backing foil.

We must also look at the source with respect to the neutrons, but not in the neutron absorption aspect (which is found negligible) but in the aspect of what happens to the fission fragments. Using the relativistic formula in Eq. 2.7 one can obtain the speed in the laboratory system and we thus find a rough estimate to the upper speed limit of the fission fragments to be about 20 mm/ns. As mentioned before, almost all neutrons are assumed to have been emitted within $4{\cdot}10^{-14}$ s after scission, which thus gives an upper estimation of how far the fragments have reached after all prompt neutrons have been emitted: $4{\cdot}10^{-14}$x20 mm/ns=0.8 μm.

Since the gold layer is approximately 2.6 μm thick we can thus infer that the fragments have not left the source at the emission of the neutrons, meaning that we can view the source as being symmetric. The platinium layer on the backside of the activity is thus assumed to be equivalent to the gold cover and its actual thickness is not important as long as it is not much thinner than the gold layer.

In Appendix A there are some data on ^{252}Cf and Fig. A.1 shows a schematic figure of our source.

Chapter 5

Experimental Setup

The experiment was carried out at Max-Lab, Lund, which meant that we had the oppertunity to use some of their state-of-the-art equipment. Most valued was their Data Acquisition System (DAS), which rendered us to perform multichannel analysis.

The experimental setup is shown in Fig B.1 in Appendix B and in Appendix C all the constituent parts are listed. We begin discussing some of the parts before looking at the whole system.

5.1 Important Parts of the Experimental Setup

5.1.1 Fission Fragment Detector

As a fission fragment detector, we used an EG & G Ortec F-series heavy ion partially depleted silicon barrier detector, specially designed for heavy ion spectroscopy. Some data for this detector are shown in Table 5.1.

The detector and the source were placed in a vacuum chamber, with a preassure of about 1-2 $\cdot 10^{-4}$ mbar, thus avoiding the preassure region 10^{-3} - 1 mbar in which, according to the manufacturer, surface breakdown is likely to occur. The distance between the source and the detector is of course a critical parameter. The longer the distance, the better the angular resolution. However, the time resolution will worsen due to the fact that the light and heavy fission fragments have different speed and in our analysis we do not discriminate between them. The

Table 5.1: Some data for the fission fragment detector.

Active area (circular)	300 mm^2
Sensitive depth	60 μm (14 mg/cm^2)
Electrode thickness (gold) on entrance window	40.0 $\mu g/cm^2$
Capacitance	540 pF

distance chosen was about 2.4 cm and the source was centered in front of the detector.

The proper operation of semiconductor detectors depends on the fact that they are made from extremely pure (impurities of the order of parts per billion), near perfect, single crystals of silicon (or germanium). However, when a detector is exposed to radiation, some damage to the lattice will take place due to the disruptive effects of the radiation, i.e. *radiation damage*. The damages are dependent upon the type of radiation, increasing with the ionization density.

Radiation damage for fission fragments is a major problem. The most common type of radiation damage is the Frenkel defect, in which a silicon atom is displaced from its equilibrium site to an interstitial position. The resulting vacancy-interstitial pair acts as a charge carrier trapping site, and thus reduces the charge collection efficiency which, decreases the energy resolution. Also, radiation damage increases the leakage current which decreases the electric field in the detector and thus futher decrease the charge collection efficiency.

By monitoring the leakage current,[1] one can get an idea of the status of the detector. One way of temporary avoiding the problem of radiation damage is to increase the bias voltage since this will improve the charge collection. The restrictions of this method is basically put by the upper limits of the HV power supply and the preamplifier used. This method of raising the bias voltage was used in our experiment and in order to get the same electric field in the detector when the HV was raised, we used an oscilloscope on which the the pulses from the α-particles, also emitted by ^{252}Cf, were well defined and could thus easily be adjusted to a given pulse height.

In Fig. 5.1 and Fig. 5.2, fission fragment pulse height spectra[2] from the beginning and from the end, respectively of the measurements are shown and the total exposure time between them is approximately 135 h during which some $220{\cdot}10^6$ fission fragments and some $3.5{\cdot}10^9$ α-particles have reached the detector .

Comparing Figs. 5.1 and 5.2, we see that the spectra do not differ significantly (the pulse heights in Fig. 5.1 are though a little bit higher, but that is of no importance in our experiment) and we therefore conclude that the method of raising the bias voltage worked properly.

Since we were to make an *absolute* efficiency calibration, we must be certain that our TOF system is triggered only by fission fragments and not by any α-particles, thus the fission detector must be able to clearly discriminate between these two types of radiation. In Fig. 5.3 and Fig. 5.4, the ungated[3] versions of the spectra in Figs. 5.1 and 5.2

[1] Displayed by the HV powersupply used.

[2] High pulse height corresponds to the light fission fragments.

[3] The two α-peaks correspond to single and double (i.e pileup in the detector) α-pulses.

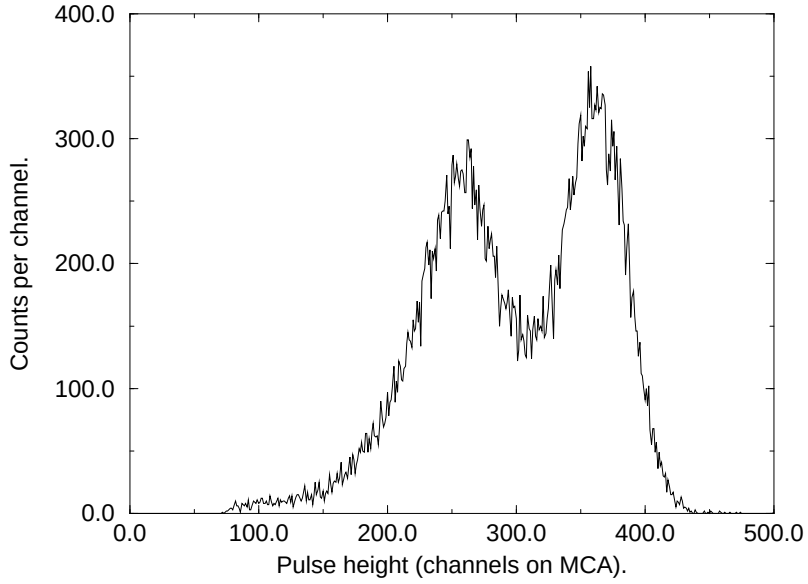

Figure 5.1: Gated fission fragment pulse height spectrum taken during 100 s at the beginning of the experiment. Applied bias voltage: 420 V, leakage current 3.01 μA.

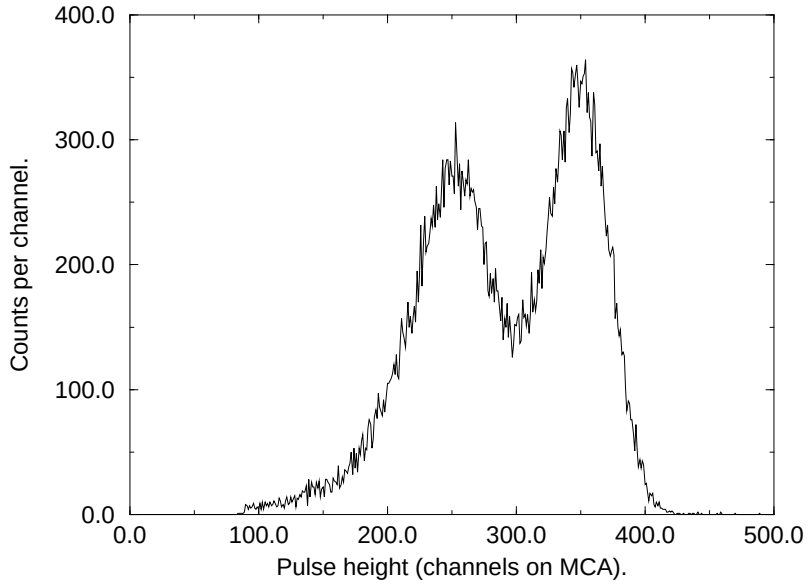

Figure 5.2: Gated fission fragment pulse height spectrum taken during 100 s at the end of the experiment. Applied bias voltage: 1234 V, leakage current 11.80 μA.

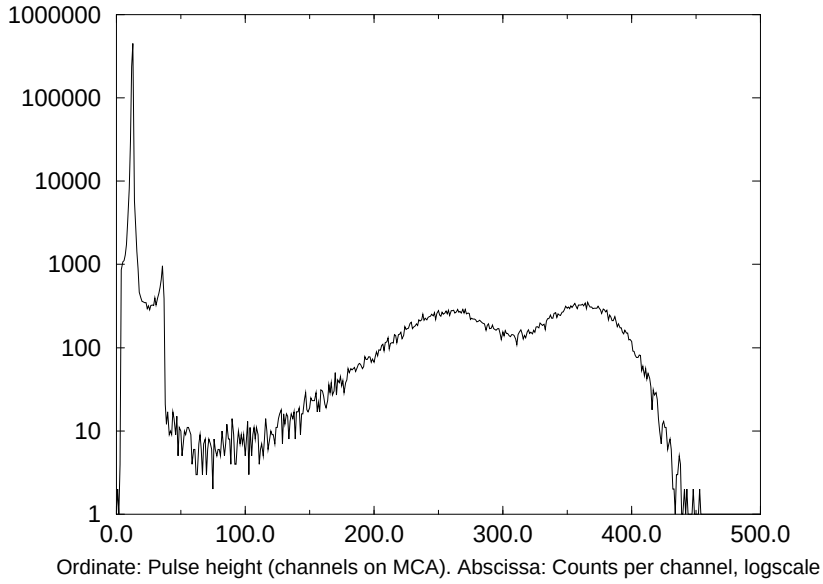

Figure 5.3: Ungated fission fragment pulse height spectrum taken during 100 s at the beginning of the experiment. Applied bias voltage: 420 V, leakage current 3.01 μA.

are shown and we see that there is a very clear seperation between the α-particles and the fission fragments. Note also that at the position of the hardware cut, i.e., around channel 90, the count rate is small compared to that of the bulk of the fission fragments which means that any small drifts in the applied threshold will be of minor importance. The existence of counts between the fragment and the α-peaks is due to edge effects, i.e. fragments clipping the detector.

We will also mention that impurities in the source, i.e. ^{250}Cf and ^{248}Cm which also undergo spontaneous fission, could effect our measurements. But due to the much smaller branching ratio for spontaneous fission (0.08%) for ^{250}Cf and the much longer half-life (approximately $3.5 \cdot 10^5$ y) for ^{248}Cm, means that the effect of them is negligible.

5.1.2 Preamplifier

The preamplifier used in conjuntion with the silicon detector was an EG & G Ortec Model 142B Preamplifier. This preamplifier provides two outputs, one so called energy signal and one so called timing signal. The timing signal is nothing but a differentiated and inverted version of the energy signal, but the differentiation removes low-frequency noise which improves the timing resolution. After adjustment of the rise time, to make the preamplifier match the capacitance of the detector, the rise time of the negative timing signal was found to be $\sim$18 ns for both α- and fragment pulses.

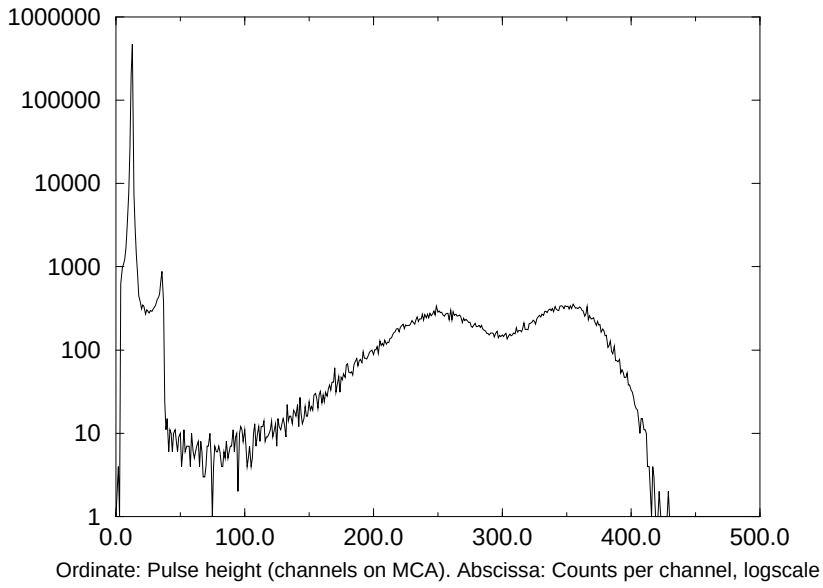

Figure 5.4: Ungated fission fragment pulse height spectrum taken during 100 s at the end of the experiment. Applied bias voltage: 1234 V, leakage current 11.8 μA.

5.1.3 Constant Fraction Discriminator

Besides the two detectors, perhaps the most important part of the setup is the constant fraction discriminator (CFD) and the one used in this experiment was an EG & G Ortec 935 Quad 200 Mhz CFD. The basic idea in a CFD is to convert an analog pulse to a digital pulse without loosing any timing information. This is done by selecting a timing point on each input pulse that is independent of pulse height, for the CFD in question this point is at the time by which the pulse has risen to 20 % of its maximum amplitude. This assumes that all input pulses are of the same shape.

It is also in the CFD that we apply our threshold, i.e. in order for the CFD to produce an output pulse the amplitude of the incoming pulse must be above a certain height. The CFD is thus *pulse height sensitive* in contrast to the ADC used with the neutron detector which is *charge sensitive* and this would, as shall be seen induce some problems.

Whenever experiments in nuclear physics are undertaken, one almost always encounters problems concerning pile-up and deadtime. The underlaying causes are the fact that the pulses from a detector are randomly spaced in time. This randomness means that there exists a probability of having two or more pulses ariving at the same time. The term pile-up usually refers to the addition of pulses in the detector itself and in subsequent amplifiers, whereas deadtime usually refers to logical modules and their 'dead time' during their pulse processing, but the distinction between them are not clear.

The two most important factors effecting pile-up/deadtime is the count rate and the length of the pulses. Using simple statistics one realises that high count rates and long pulses will introduce a lot of deadtime/pile-up whereas low count rates and short pulses will minimize the effects of deadtime/pile-up. Since it can be hard to correct for deadtime/pile-up one usually wants to minimize the risk for it. One should always try to assess the count rates in ones experiment and looking at dead times and possible deadtimes adjustment, the CFD plays an important role.

This is, and here we make the picture simple, because in all the modules following the CFD we can, by adjusting the width of the digital pulses, by inhibiting the right modules or inserting delays etc., avoid[4] deadtime problems. However before the CFD we do not have the same possibilty of controlling the pulses and we must therefor make some assessments. First, the CFD itself is in an updating mode which means that if the energy condition for producing an output pulse fulfils, by a second pulse, during the output of a previous pulse, the first output pulse will be extended a time *width* from the time of arrival of the second pulse. *width* is the user specified length of the ouput pulse. If an input pulse does *not* fulfil the energy condition there will of course be no output pulse but the CFD will neverthless have been busy.

We thus see that the critical factors that effect the deadtimes are the count rates as seen by the CFD. We look at these deadtimes for each detector seperately.

- If we look at the count rates of the gated and the ungated spectra in Figs. 5.1 and 5.3 we find them to be 8006 Hz respectively 460 Hz, their quotient being (17.40±0.08) Hz, while the theoretical quotient is supposed to be 16.18±0.01, we have thus measured too few fission fragments, either because there are some fission fragments below the threshold, and thus not counted in the gated spectrum, or because of deadtimes in the CFD. Whatever the reason is, this effect is of no concern, because (as long as this loss of fission events is independent of neutron emission, which seems like a reasonable assumption) of the simple fact that if there is no registered fission event there can be no coincidence between a neutron and a fission fragment.

- The deadtime-pile-up effects in the neutron detector are of much more concern. The reason for our concern is as follows: If a fragment is detected in the fission detector and thus produces a *possible start*, $= N_f$, then we want the neutron detector to be able to detect the, possibly impinging, coincident gamma. If the

[4]Or at least control, in our experiment the setup is trimmed to avoid any deadtime-pileup problems.

neutron detecor (or the neutron branch of the experimental setup) is dead, then that event would have been lost and our measured efficiency of the neutron detector would have been too low. Thus, we must try to estimate the actual count rate in the detector to see whether or not deadtime corrections have to be done.

There are three contributions to the count rate in the neutron detector: neutrons and γ:s from the source and the background. An estimation of the total number of neutrons that impinges on the detector per second are 18 (370000*0.0309*430·10^{-6}*3.757) and an estimation of the total number of γ:s that impinges on the detector per second is 50 (370000*0.0309*430·10^{-6}*10), the figures refering to activity, fission branch ratio, solid angle factor and neutron multiplicity respectively γ multiplicity [Bru 82]. Note that these figures are whithout any threshold. As far as the background is concerned it is for this size of detectors estimated to be of the order of 100 Hz [San 97]. These low count rates together with the fast pulses from the scintillator thus means that no deadtime correction had to be done.

5.1.4 Neutron Detector

As a neutron detector we used a 20x20x10 (h×w×d) cm NE-213 liquid scintillator. This detector is an exact copy of one of the nine cells in one of the two big neutron detectors at present used at MAX-LAB [MAX 95]. The distance between the source and the center of the detector was 277±1 cm which is about the same distance as used in the ^{4}He(γ,n) experiment [5].

The detector was fed with -2300 V which then produced large enough pulses so a preamplifier was not needed. The rise time of the pulse was about 8 ns and seemed to be independent of the pulse height. For more information about the detector see chapter 3.

5.1.5 Pulse Shape Discriminator (PSD)

As can be seen in our experimental setup, no PSD module was used, which was due to the low count rate in the neutron detector (∼200 Hz). However, prior to the experiment we tested the neutron detector together with a PSD module to make sure no deoxygenation was needed.

The PSD module used was a Link Systems PSD Model 5010 and a very simple description of its mode of operation is as follows. The input pulse is integrated for two different times, one short (∼25 ns) and one long (∼500 ns). The results of the integrations are compared

[5] They used 2650 mm.

and an otput pulse produced whose height and polarity is correlated to the "quotient"[6] of the two integrations. This output pulse is often labelled 'Y'. The PSD module also produces a pulse, often labelled 'X', proportional the original pulse height. If these pulses are fed to an oscilloscope in X-Y scatter mode we should, if the detector has any pulse shape discrimination properties, be able to see some bands representing the different incident particles.

When we placed a PuBe source (a strong neutron and γ emitter) in front of the detector and produced an X-Y scatter plot as described above, we got the result shown in Fig. 5.5. In this figure, we see that there is a clear seperation between the γ:s and the neutrons and thus no deoxygenation of the detector was required.

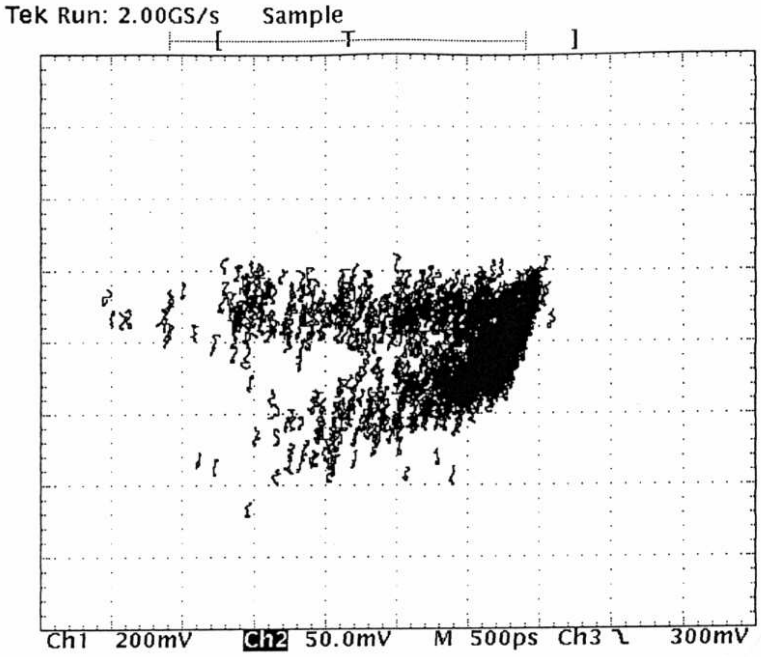

Figure 5.5: PSD spectra obtained with a PuBe source. The upper branch corresponds to γ:s and the lower to neutrons.

5.2 The whole system

The experimental setup, which can be seen in Fig. B.1 in Appendix B, can be said to consist of two branches, the fragment and the neutron branch, which then in turn each consist of two sub-branches denoted

[6]Not to be interpreted as a mathematical statement, for a true description of how this output pulse is produced see [Ada 78].

as energy and timing branch. There is also a pure physical division resulting from the fact that there was a large distance (approximately 75 m) between the experimental area and the Data Acquisition System (DAS). This division is indicated by the upper verticle dashed line in Fig. B.1 in Appendix B.

One might think that the long cables used between the experimental area and the DAS would cause a lot of problems due to attenuation, degrading of timing characteristics or noise pick-up. As far as attenuation and timing characteristics were concerned, no problems were encountered, but we did find two examples of pick-up. They manifested themself as very large increases in count rate during a very short period of time and it turned out that they were coincident with the electron beam on the MAX-II storage ringe being dumped. Since this sort of pick-up is easily detected, it was not considered to be a problem.

The lower dashed line in Fig. B.1 in Appendix B, parts, besides from the scalers S0,...,S4, the modules that are read out with the DAS from those not.

Among the logical units, the most important is the so called main AND. It is in this AND gate that the coincidence condition between the two timing pulses is checked and the condition is true if the timing pulses have arrived within approximately 700 ns. When there is a coincidence event the main AND will start the DAS via the so called X-trig signal which in turn generates an inhibit signal during the processing time (700-1500 μs depending whether or not the scalers are being read out). The inhibit signal is fed back to the main AND which thus will be inhibited until the processing by the DAS is done. The main AND also generate gates for the TDCs and ADCs and because the ADCs are self-inhibiting[7], it is important that they are gated only by the main AND.

Besides the TDCs and ADCs the DAS reads out 5 scalers, denoted as S0,...,S4. These count the number of pulses at various positions in the setup and the by far most important of them is S0 since this gives the *number of possible starts* = N_f, i.e. the number of fission events above the threshold in the fission detector, which enters into the forthcoming analysis.

[7]Once they have been gated they are inhibited until they are read out by the DAS.

Chapter 6

Experiment

In Fig. 6.1, the main features of the experimental setup are shown. The experiment consisted of a total of nine runs, seven with different angles Θ , one run in which the veto detector was placed in front of the neutron detector and one run with a lead shadowing cone placed between the source and the neutron detector, the so called background-run.

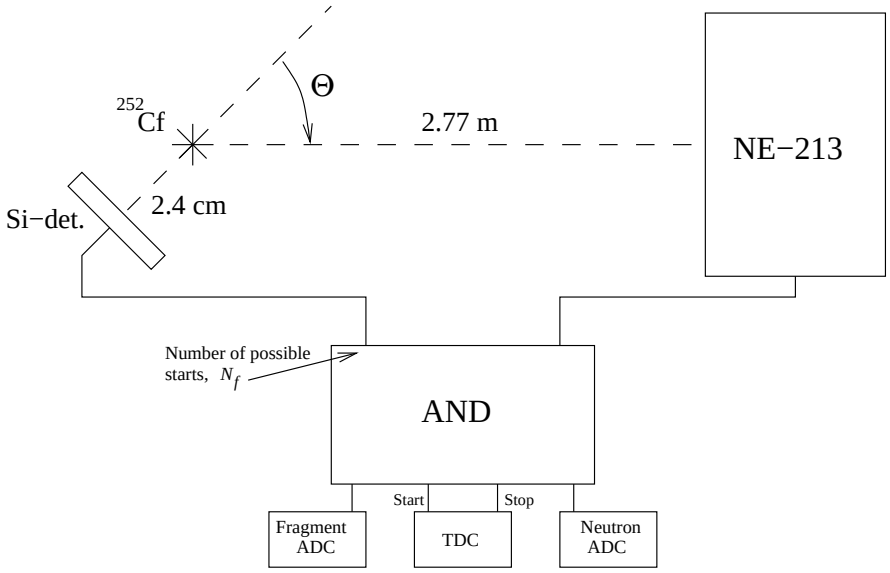

Figure 6.1: Simple picture of the experimental setup.

Due to radiation damage in the silicon detector, each run consisted of 4-8 indiviual sub-runs with the silicon bias voltage being adjusted in between these sub-runs. In every sub-run, the following information was obtained from the DAS and saved to magnetic tape:

- TDC spectrum, also called TOF spectrum.
- ADC spectra for each detector.

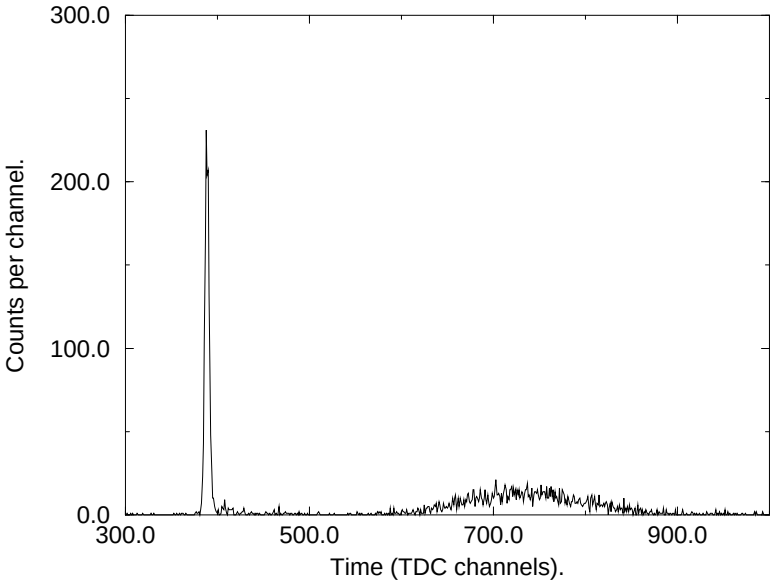

Figure 6.2: Original TDC spectrum from a typical run, this run having $\Theta = 0^\circ$ and acquisition time 3.0236 h.

- Scalers; S0,...,S4.

In Figs. 6.2, 6.3 and 6.4, the original TDC, neutron-ADC and fragment-ADC spectra for a typical run is shown.

Note that in the fragment-ADC spectrum, the ratio 'heavy' to 'light' has interchanged compared to the non-coincidence spectrum in Fig. 5.1. This is a consequence of the higher neutron yield from the light fragments.

In the TOF spectrum, the highest peak corresponds to the so-called γ-flash, which makes it possible to put the time scale on an absolute basis, and the small bump corresponds to neutrons. In Fig. 6.5 an enlargement of the interesting parts of a TOF spectrum is shown[1] and besides the γ-flash and the neutron bump we note the small peak just to the right of the γ-flash. Being analysed the peak is found to be $\approx$5 ns behind the γ-flash. The peak is believed to be a mixture of scattered photons and delayed photons, cf. Fig. 4.3. In Fig. 6.5, we also see that the lowest intensity is found to the left of the γ-flash and these counts consists only of random coincidences.

6.1 Background

The neutron background consists of random coincidences and scattered events, i.e. a neutron corresponding to the triggering fragment is detected after having scattered into the detector. In order to estimate

[1] Fig. 6.5, is a summation of the spectra taken at $\Theta = 0^\circ$ and thus represents the bulk information in this experiment and thus refered to as the main run.

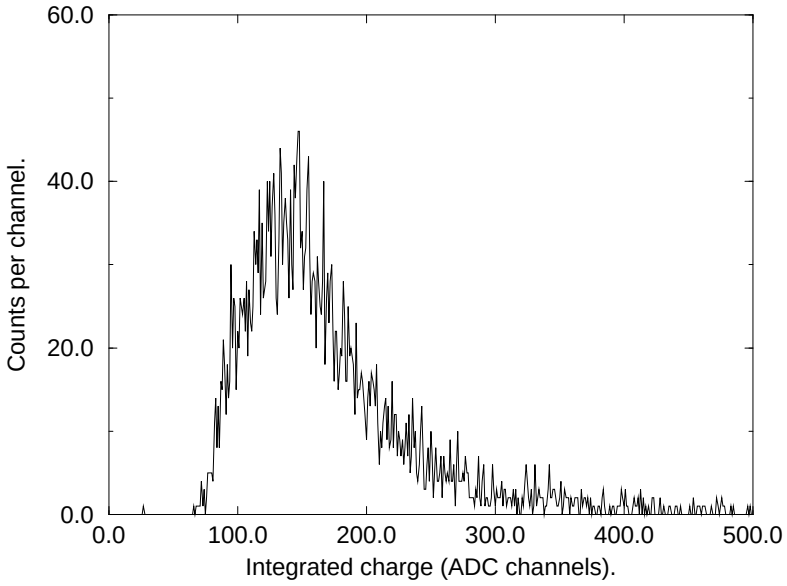

Figure 6.3: Original neutron ADC spectrum from a typical run, this run having $\Theta = 0^\circ$ and acquisition time 3.0236 h.

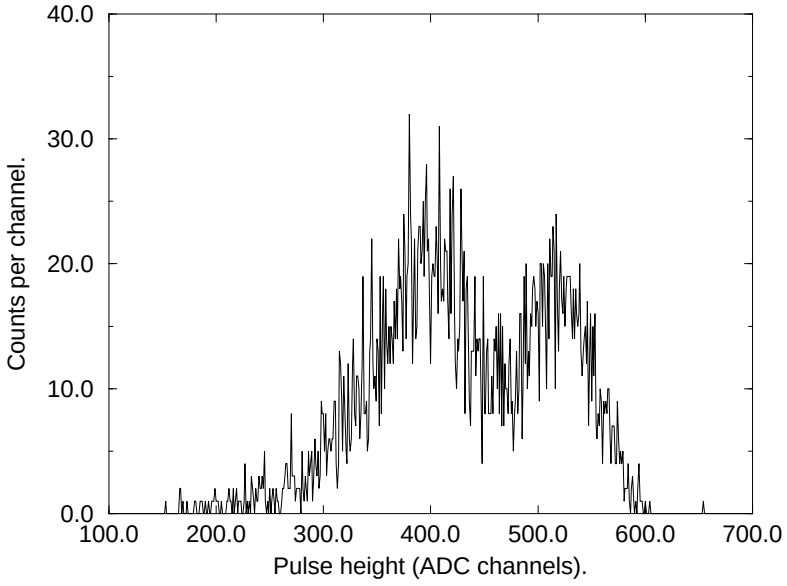

Figure 6.4: Original fragment ADC spectrum from a typical run, this run having $\Theta = 0^\circ$ and acquisition time 3.0236 h.

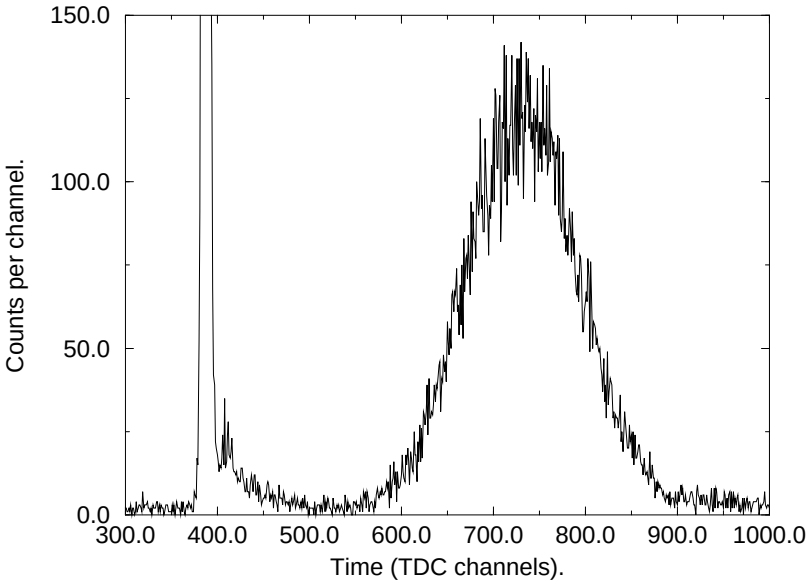

Figure 6.5: Enlargement of the TOF spectrum from the main run, i.e. Θ=0°.

the scattered background, a 48 cm long shadowing lead bar was placed between the source and the detector.

Using $\sigma_t \approx$7 barns and $\mu \approx$0.7 cm^{-1} for the total cross section and the absorption coefficient, we find that the neutron and the photon transmission in the lead bar is very close to zero. Thus any events found in the TOF spectrum are believed to be either random coincidences or scattered events. In Fig. 6.6, this TOF spectrum is shown. Comparing this with Fig. 6.5, it seems like the peak of the neutron bump in the background-run is a little bit delayed.

The random coincidence rates in the different runs were calculated and found to be equal, within the margin of error, to that of the background-run. This means that the background-run can be used as a representative of the total background. As will be seen, the background is assumed to be angular independent, which is perhaps not the most appropiate assumption but since the effect of the background is rather small, a bigger error can be accepted.

6.2 Calibrations

Two different types of calibration were performed, time calibration of the TDC and energy calibration of the neutron detector. The TDC calibration is a straightforward procedure using an EG & G Ortec Time Calibrator and the time conversion factor (i.e. time per TDC channel) was found to be the same before and after the experiment (248.9±0.1 ns).

The energy calibrations were done using γ:s from a PuBe and a

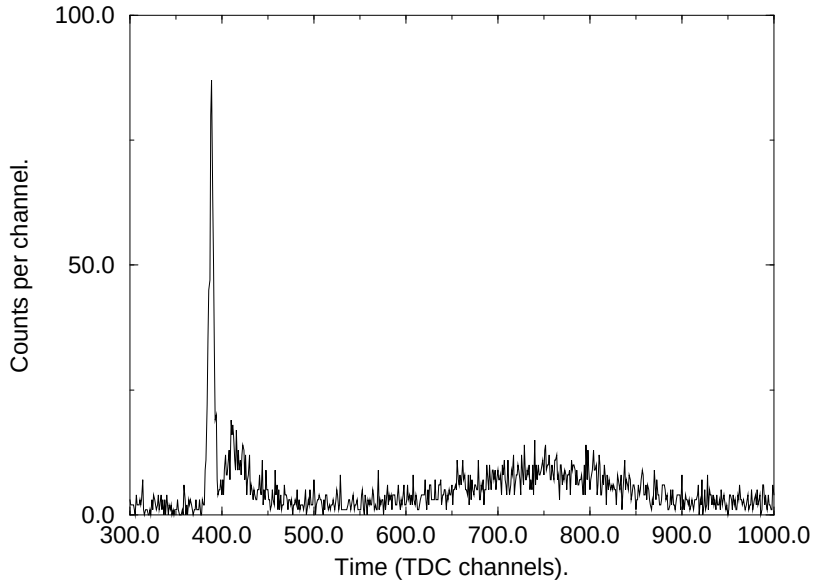

Figure 6.6: TOF spectrum acquired with a lead bar placed between the source and the detector.

^{232}Th source. Due to the lack of high-Z atoms in the scintillator, no photo peaks occured, thus the Compton edges had to be used. In Fig. 6.7 and Fig. 6.8 these spectra are shown and we clearly see the Compton edges from the 2.614 MeV respectively 4.44 MeV γ:s and following the method suggested by Knox [Kno 72], the half height of the distributions are taken as corresponding to the Compton edge. Besides these two points, the zero cross-over point was also used and these three points were fitted to a straight line.

The energy calibration was to determine the threshold but the fact that the CFD is pulse height sensitive and the neutron-ADC is charge integrating results in a widening of the observed threshold in the spectra, and, due to the presence of photons, a lowering (compared to what would have been the case if no photons were present) of the observed threshold in the coincidence spectra. These difficulties in determining the so called hardware threshold lead us to, in the analysis, apply a software threshold in the neutron-ADC spectra.

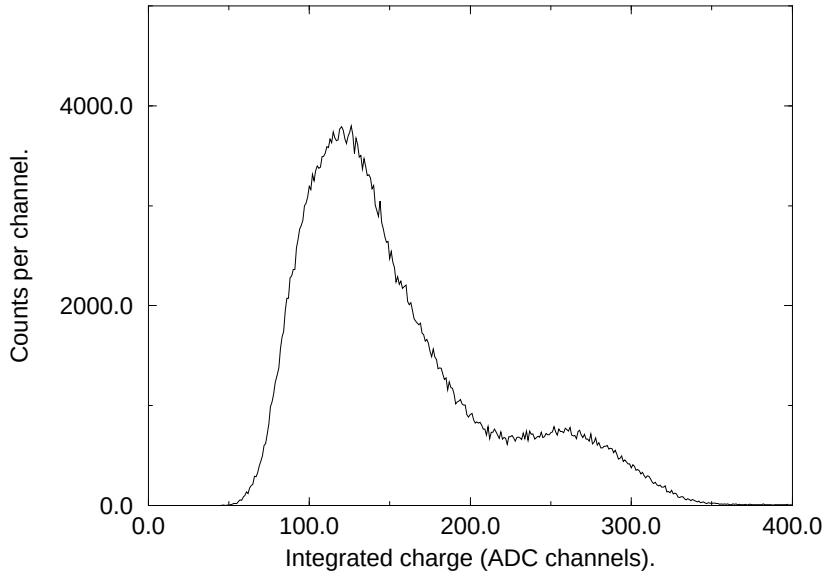

Figure 6.7: Spectrum from a ^{232}Th source, the Compton edge from the 2.614 MeV photon clearly seen.

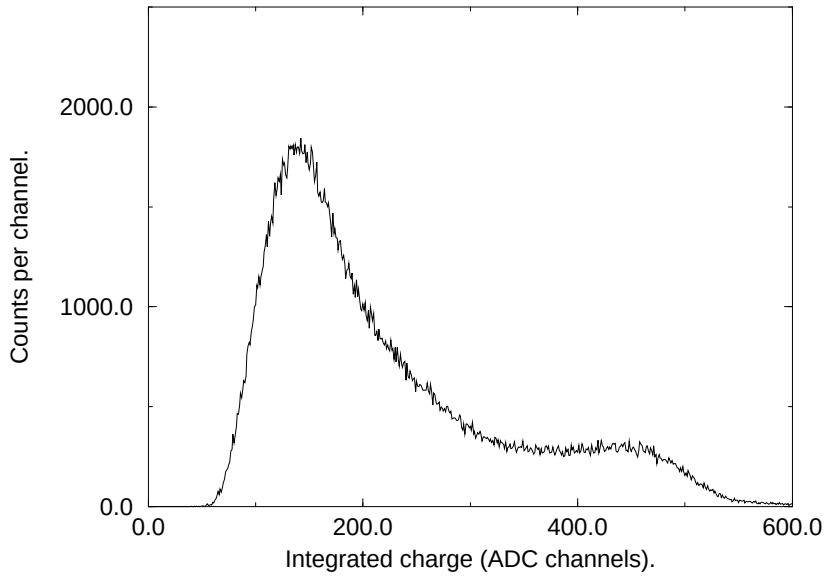

Figure 6.8: Spectrum from a PuBe source, the Compton edge from the 4.44 MeV photon clearly seen.

Chapter 7

Data Analysis

As pointed out in the previous chapter, a software threshold in the neutron-ADC spectra was applied to our data, the effect of this cut can be seen in Figs. 7.1, 7.2 and 7.3, which are the same spectra as in Figs. 6.2, 6.3 and 6.4. Since a rather large fraction of the information was lost because of the cut, the uncut spectra were also analysed in parallel[1]. Due to the fact of a strong threshold dependency in the neutron detection efficiency, cf. Eq. 2.10, the stability of the threshold was checked and confirmed.

Once the TOF spectra from the individual runs where added, the γ-flash was analysed and a Gaussion fitted to it. Using the mean, *gpos*, of the Gaussian, the TDC channel corresponding to the time of the fission event can be calculated by

$$zerochannel = (gpos - \frac{fp}{c{\cdot}conv}) \tag{7.1}$$

where *conv* is the time conversion factor. The Gaussion also provided us with the FWHM of the γ-flash (found to be $\approx$1.5 ns), which is a measure of the timing resolution, see section on Timing resolution. Using Eqs. 2.7 and 7.1, a conversion from TOF spectrum to an absolute energy spectrum was undertaken and due to the nonlinear relationship between the tof and E_n in Eq. 2.7, the resulting energy spectrum needed to be binned in bins of equal width (bin width 0.5 MeV).

The resulting neutron energy spectra were then normalized to the same number of possible starts, N_f, and the neutron energy spectra taken at the angles 0°, 52°, 72° and the background-run, can be seen in Fig. 7.4. Three of the runs were recorded at a significantly different time than the others and due to drifts in the PM-tube voltage, about a 6% increas in the number of neutrons was observed and later corrected for.

[1]The two sets are referred to as cut and nocut

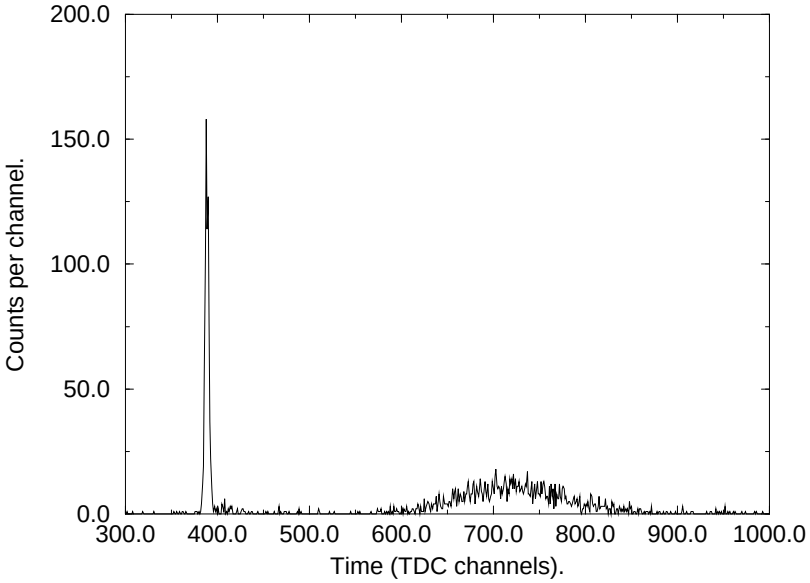

Figure 7.1: Same TDC spectrum as in Fig. 6.2, but with a software cut.

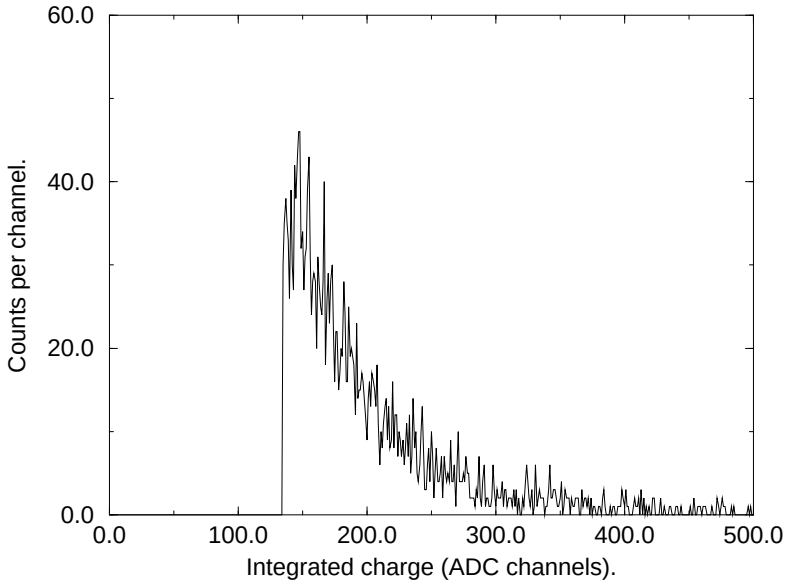

Figure 7.2: Same neutron-ADC spectrum as in Fig. 6.3, but with a software cut.

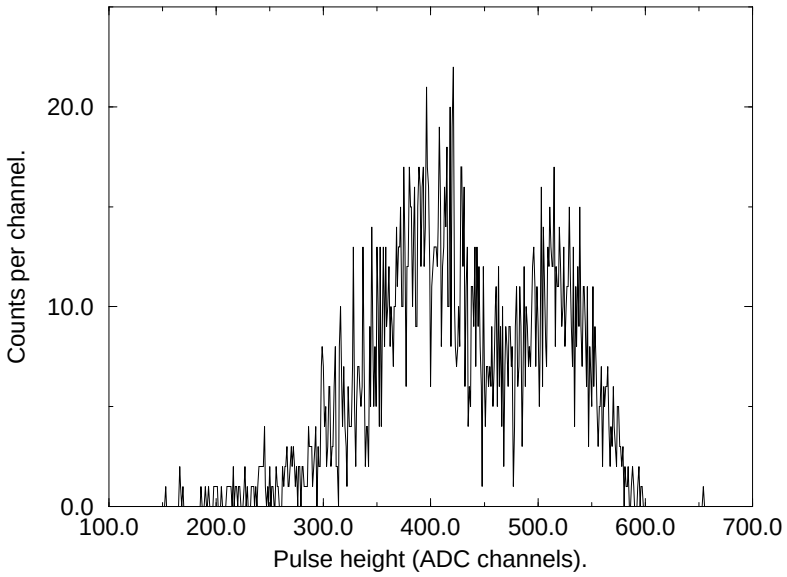

Figure 7.3: Same fragment-ADC spectrum as in Fig. 6.4, but with a software cut.

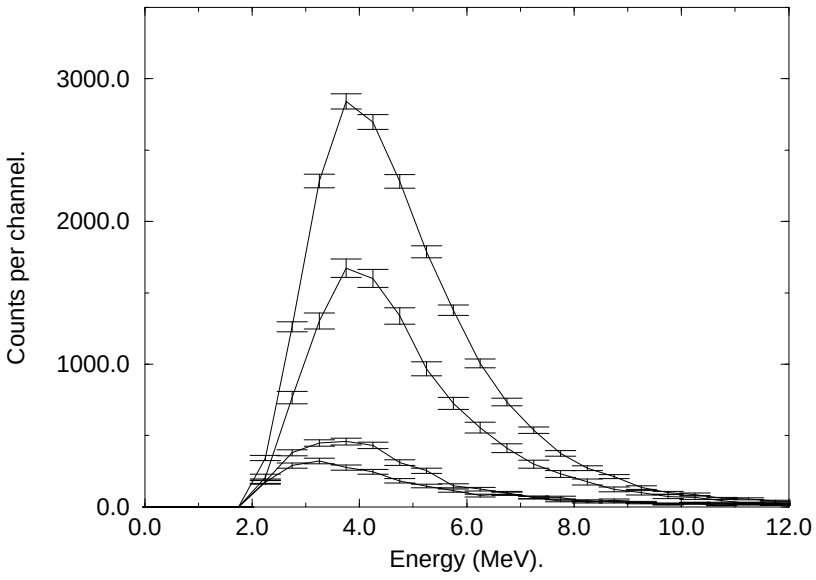

Figure 7.4: Normalized neutron energy spectra taken at angles (starting from the top), $0^{\cdot}$, 52°, 72° and the background-run.

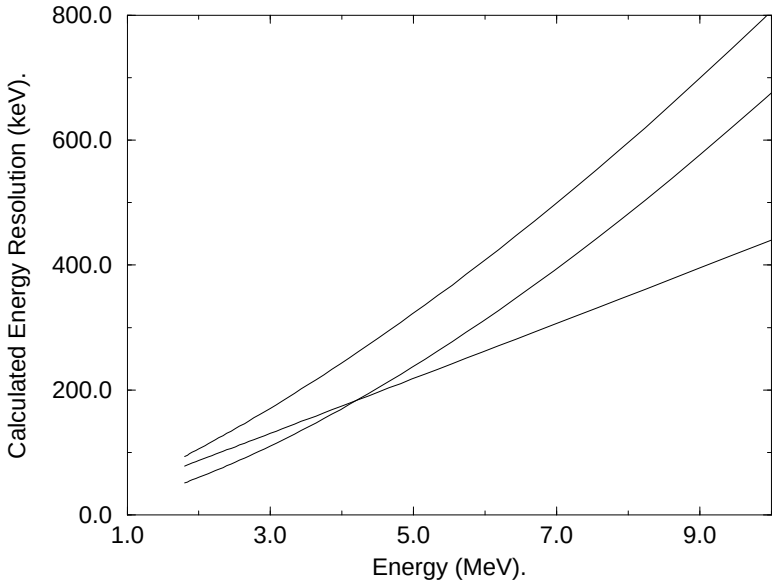

Figure 7.5: Energy resolution as a function of energy, using FWHM$_{fp}$ ≈6 cm and FWHM$_{\gamma}$ ≈1.5 ns. From top(at high energies): total, only FWHM$_{\gamma}$ and only FWHM$_{fp}$.

7.1 Timing Resolution

In a TOF experiment, the energy resolution is determined by the timing resolution, thus by increasing the flight path, better energy resolution is obtained. Some of the factors that determine the timing resolution are: different fission fragment velocities, timing uncertainties inherent in the detection system, finite width of the TDC channels and the difference in tof depending on where in the neutron detector the interaction occurs. The FWHM of the γ-flash includes all effects but the last.

In order to estimate the last effect, one can calculate the average scattering position of neutrons in the detector and then by the use of statistics, obtain the corresponding FWHM of this effect [Bow 62], however a much more simple way is to treat the effect as an uncertainty in the flight path. If we were to use the thickness of the detector as FWHM$_{fp}$, it would be too pessimistic, but reference [Bow 62] suggests for a FWHM$_{fp}$ for a 5 cm thick detector to be about 3 cm. Thus as an approximation we use, for our 10 cm thick detector, FWHM$_{fp}$ ≈6 cm. Note that the effect of a neutron hitting the front face of the detector at various positions does only introduce a very small error in the flight path, thus it can be neglected.

The FWHM$_{\gamma}$ was found to be about 1.5 ns and using simple error propagation the energy resolution (in terms of FWHM) obtained can be seen in Fig. 7.5.

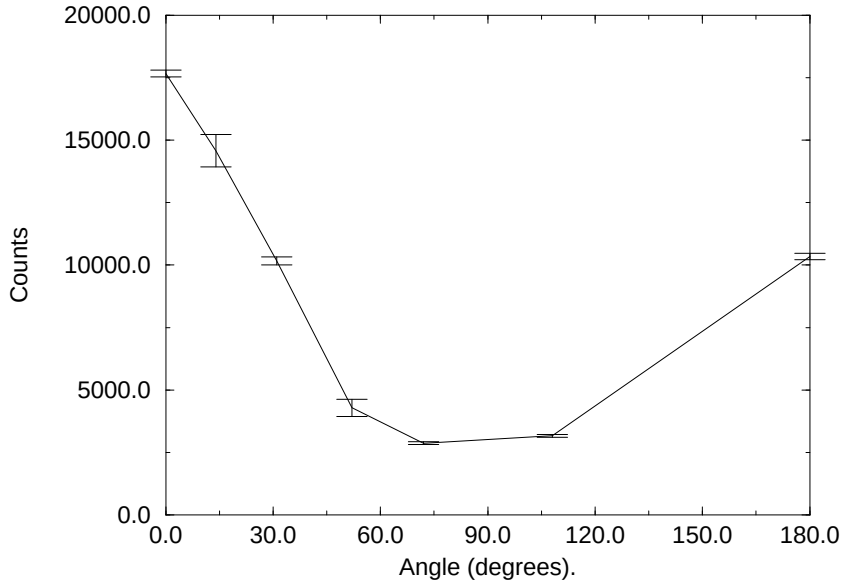

Figure 7.6: The integrated angular distribution (2.75-8.75 MeV)

7.2 Angular Distribution

This part turned out to introduce some unforseen difficulties due to the limitations of the experimental setup, and in order to obtain reliable results, it had to be treated in a most pragmatic way. Not surprisingly, the largest fraction of the total error in the results originates from effects of the angular distribution.

In Fig. 7.6 the integrated angular distribution is shown. Integrated means here the total number of neutrons in the energy region 2.75-8.75 MeV. First note that the low number of counts at angle Θ=180° is because of absorption in the fission detector (i.e. the neutrons have to travel through the fission detector to reach the neutron detector), second note the difference in the number of counts at angles Θ=72° and Θ=108°. Since we expect a symmetric distribution around 90°, this difference is interpreted as an error in the determination of the angles and the angles were thus shifted[2] 2° (the Θ=0° and the Θ=180° were not shifted since they were well determined).

The angular distribution is, as can be seen in Fig. 4.5, energy dependent, thus the angular distribution was analysed for every single 0.5 MeV bin, except for energies higher than 5.5 MeV (poor statistics), thus the energy intervall 5.5-9 MeV was treated as one unit. The background was subtracted (assumed to be angular independent) and then the procedure to fit Legendre polynomials, according to Eq. 4.10, was started.

Because of the expected symmetric distribution, the measurement

[2]The "nice and smooth" argument, see ahead in this section, can be used in justifting the shift; the shifted fitts are "nicer and smoother" than the unshifted.

at angle 108° was, after being shifted 2°, used as a data point at 70°, furthermore we constucted a data point at 90° by calculating $y(90°) = 0.75y(74°) + 0.25y(background)$ where $y(\Theta)$ is the number of counts at angle Θ in any of the energy intervals. This forces the polynomials to have there minimum at 90°, which is a reasonable assumption.

Thus we ended up with a total of seven angles 0°, 16°, 33°, 54°, 70°, 74° and 90°. Given seven angles, we can at most have six Legendre polynomials in the series and this polynomial will exactly go through all the data points, a rather unrealistic situation since this polynomial very often will have unrealistic structure. Thus one way to separate a good fit from that of a bad is to require the good to be "nice and smooth", also, refering to Occam's razor[3], there should be as few terms as possible. Thus, these handwaving arguments finaly made us believe that three Legendre polynomials was sufficient. Thus, to conclude, the measured angular distributions are finally fitted to a function of the form;

$$W(\Theta) = const(1 + K_2P_2(\cos\Theta) + K_4P_4(\cos\Theta) + K_6P_6(\cos\Theta)) \quad (7.2)$$

and from Eq. 7.2 the geometrical enhancement factor,

$$GEO(E) = (1 + K_2 + K_4 + K_6), \quad (7.3)$$

is calculated.

In Figs. 7.7 and 7.8, some of the obtained fits are shown. Note that the K_i factors are functions of the true angular distribution and on the geometry.

The calculations are nothing but solving a system of linear equations, when a six term polynomial is fitted, there exists a unique solution (unless the determinant of the matrix is zero), and if polynomials of lower order are fitted the system is over-determined, but a solution can be obtained using least square methods. If we regard the solutions obtained by the least square method as 'unique' we can conclude that, to every measured angular distribution there exist a unique GEO factor. However this does definitely not mean that no error is present in the GEO factor. The most common way in estimating the error is by so-called experimental error calculation, which we also used.

The experimental error calculation was done by generating Gaussian distributed errors with mean 0 and with each datapoints' indiviual standard deviation. These errors were then added to the corresponing data point and a new calculation of GEO was done. This was done a hundred times and the observed standard deviation in GEO was taken to be the error wanted. The error was found to be ∼10 %, which thus is by far the biggest error in our calculations.

[3]'It is vain to do with more what can be done with fewer', William of Occam (1290?-1349).

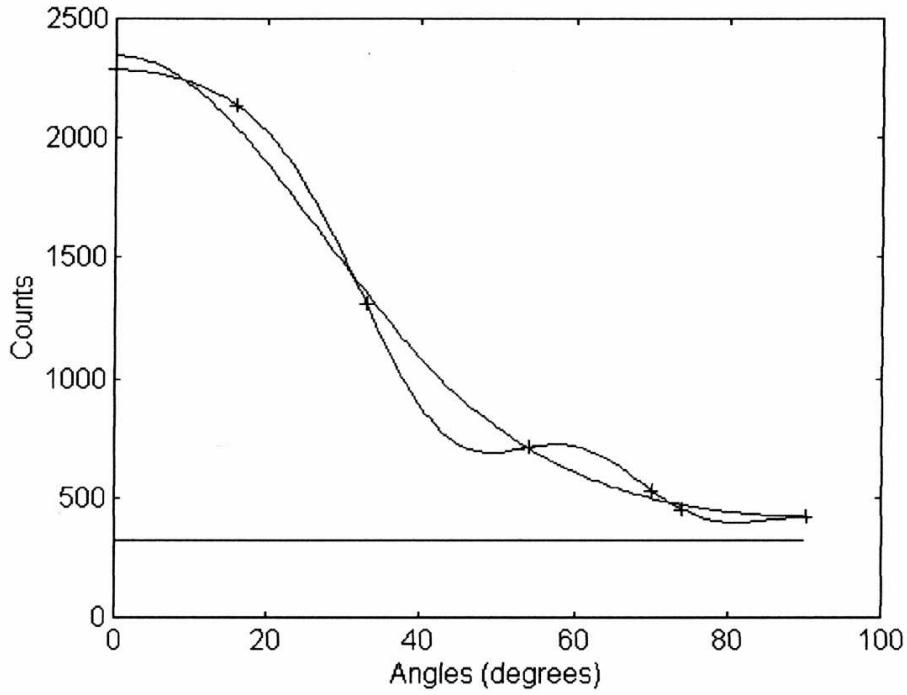

Figure 7.7: Fitted Legendre polynomials using three terms and using six terms. Note that the polynomial using six terms goes exactly through all seven datapoints. This is for enegy 3.25 MeV and yields GEO=4.0. If the six-term polynomial were to be used the GEO factor would have been 3.9. The straight line is the background, assumed to be isotropic

7.3 Absolute Efficiency

Everything can now be put together and the absolute efficiency ϵ is calculated by

$$\epsilon = \frac{Mainspectrum - Background}{N_M^c(E) \cdot 0.5 \cdot \overline{\nu_p} \cdot GEO \cdot N_f \cdot \frac{\Delta\Omega_n}{4\pi}}, \tag{7.4}$$

in which $N_M^c(E)$ is the corrected Maxwell energy distribution ($T_M = 1.42MeV$) as recommended by [IAEA 86], $\overline{\nu_p}$ is the total number of emitted prompt neutrons, $GEO(E)$ is the geometrical enhancement factors, N_f is the number of possible starts[4], $\frac{\Delta\Omega_n}{4\pi}$ is the solid angle subtended by the neutron detector divided by 4π and the 0.5 factor is a bin factor due to the fact that the measured spectra are binned in 0.5 MeV bins.

Because of the fact that there are *two* fission fragments emitted per fission event, there were some discussion as to whether or not a factor

[4]For the *main spectrum*, all other spectra are normalized to this number.

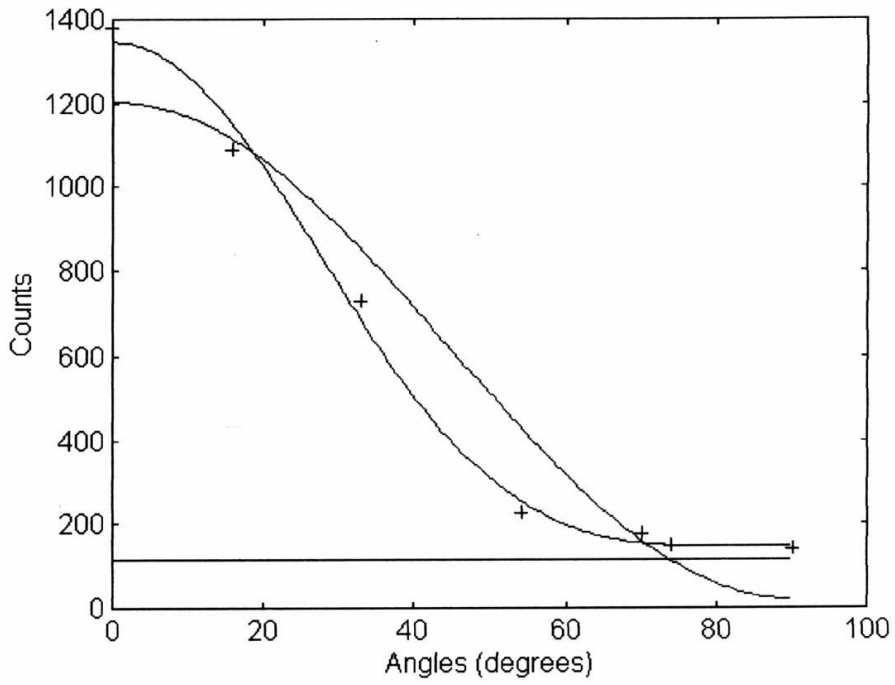

Figure 7.8: Fitted Legendre polynomials using three terms and using one. Note the bad fit when only one term is used. This is for energy 5.75 MeV and yields GEO=5.0. If the one term polynomial were to be used the GEO factor would have been 3.6. The straight line is the background, assumed to be isotropic.

of two should appear in the calculations. It does not appear due to the fact that the neutrons are measured in *coincidence* with a fragment and when *one* fission fragment is detected there are a total number of $\overline{\nu_p}$ neutrons emitted.

In Fig. 7.9 the resulting absolute efficiency obtained using Eq. 7.4 is shown.

7.4 Threshold

The obtained efficiency curves are of course without interest if the applied threshold is unknown. Using the energy calibration carried out the software threshold was found to be;

Software threshold: 950±30 keVee[5].

As can be seen in Fig. 6.3 the hardware threshold is not sharply defined, but as is customery, the half height is assumed to be an estimate of the

[5]See below for an explanation of ee.

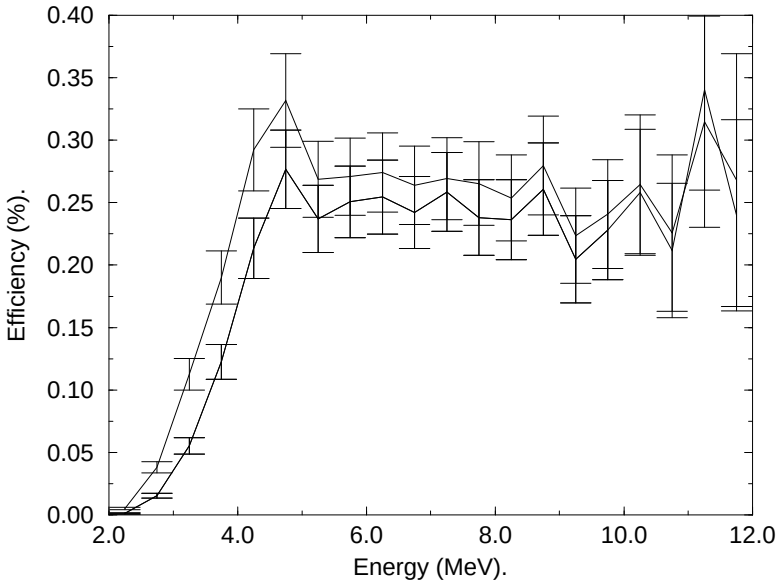

Figure 7.9: The absolute efficiency obtained using Eq. 7.4, the top curve is the uncut data and the bottom is the cut data.

actual threshold[6]. Thus, using the channel corresponding to the half height of the distribution, we find the hardware threshold to be ≈600 keVee.

The here stated thresholds are what is refered to as *electron equivalent*, energy, ee, and in order to translate this into *neutron energy* we use Eq. 2.11 and the resulting thresholds are (with reference to neutron energy)

Software threshold: 2.75±0.15 MeV.
Hardware threshold: ≈2 MeV.

7.5 Veto Detector

In this test we wanted to measure the transmission of neutrons through a 2 cm thick NE-110 plastic veto detector. The veto detector was placed just in front of the neutron detector, as it is, in a photonuclear experiment in which the large (3 by 3) neutrons detectors are used, see Fig. 1.1. The transmission is simply calculated by dividing the neutron energy spectra obtained *with* the veto detector in front of the NE-213 detector by the spectrum obtained *without* the veto detector in front. The obtained quotient is shown in Fig. 7.10. If we integrate over the energy region 2.75-8.75 MeV we find the quotient to be 0.84±0.02, only statistical errors.

When the veto detector is used in a real experiment it is usually in an anti-coincidence mode to veto against charged particles and, a thresh-

[6]At least when the effects of different pulse shapes are not present.

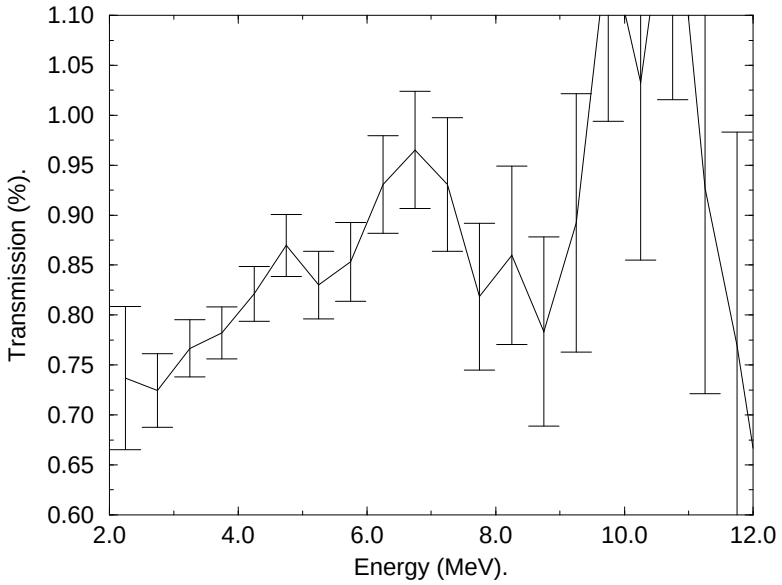

Figure 7.10: The measured transmission in the veto detector. Integrating over the region 2.75-8.75 MeV yields 0.84±0.02.

old of about 1MeVee is applied to it. That is, if a particle deposits more than 1 MeVee in the veto detector *and* is detected in the neutron detector, the event is *removed*. Such an event will *not be removed* in our experiment and we will thus measure a higher transmission than what is measured in the anti-coincidence measurements. However this discrepancy is probably negligible due to the fact that 1 MeVee corresponds to approximately 3 MeV neutron energy which means that only neutrons with energies exceeding 5-6 MeV can fulfill the anti-coincidence condition, and as can be seen in Fig. 7.4 the number of such neutrons is not great. Futhermore, the neutron-efficiency of a 2 cm thick detector is not to be considered big (cf. our measured efficiency for a 10 cm thick detector).

7.6 Errors

The errors of most interest in this experiment are the ones in Eq. 7.4. As mentioned earlier, the biggest error is in the GEO factor, estimated to be 10%. The next biggest error is probably in the determination of the subtended solid angle $\Delta\Omega_n$ and it is estimated to be about 5%[7]. Let it also be noted that the distance used in determining the solid angle is from the source to the front face of the detector but the flight path is the distance from the source to the center of the detector.

In the corrected-Maxwell energy distribution the errors are assumed

[7]This remarkable high number is due to the quadratic dependence on a relatively small distance i.e. the side of the detector.

to be less than 2% [IAEA 86]. The error in the total number of possible starts are assumed to be zero, i.e. all, and only these pulses, are assumed to have been able to trigger the coincidence condition. The error in $\overline{\nu_p}$ is assumed to be negligible. This gives a total error in the denominator of about 11 %.

All the measured spectra have been assumed to follow Poisson statistics, which in the conjuction with the error in the denominator yields a total error in the efficiency of about 13 %. In Fig. 7.9 and Fig. 8.1 this error is completely pictured as statistical errors (i.e. has errorbars on the obtained function itself).

Chapter 8

Results and discussion

The results of this experiment are the absolute efficiency in Fig. 7.9 and the veto transmission in Fig. 7.10. In this chapter we will compare our measured values with Stanton code calculation and GEANT[1] simulation.

Starting with the efficiency, in Fig. 8.1, calculations, using the Stanton code [Cec 79], of the efficiency with a 1 MeVee threshold can be seen together with our measurements. First it can be noted that the calculated software cut applied to the data is in very good agreement with the Stanton results.

If we look at the efficiency in the region above $\sim$5 MeV we see that the Stanton calculation is about 5 percentage units higher than our measured values. Although the Stanton calculation is higher than our measured values we still believe that it is in reasonable agreement with our results. The reason for this is that if we compare them in the light of the systematic errors in the Stanton code ($\sim$5 %) and the errors estimated in our measurements ($\sim$ 13%), the Stanton calculation and our measurements are almost in agreement within the margin of error.

The large errors involved in our experiment are, due to difficulties in dealing with the effects of the angular distribution. One way of avoiding these difficulties would thus be to use either 2π or 4π geometry detector, but then other problems concerning edge effects, the influence on the neutron field, discrimination between α-particles and timing characteristics etc. are introduced.

We now turn our attention towards the transmission through the veto detector. In Fig. 8.2 our measured values together with the GEANT simulation can be seen, and we note that they agree fairly well (not paying too much attention at the low energy part due to poor statistics). Comparing the integrated, in the intervall 2.75-8.75 MeV, transmission which we found to be 0.84 ± 0.02[2], see chapter 7.5, we see that this

[1] Simulation package developed at CERN.

[2] Only statistical errors.

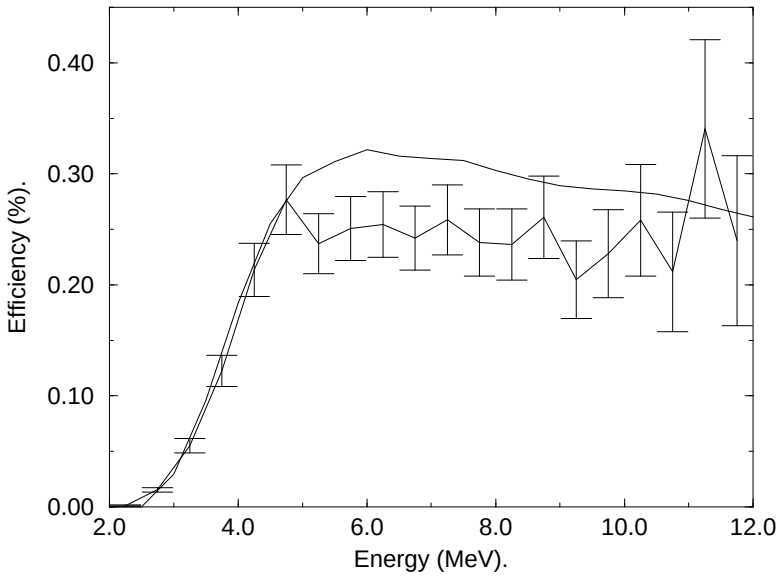

Figure 8.1: Our results for the software cut data together with Stanton code simulation with thresholds 1.0 MeVee. From [Sim 97].

agrees well with the GEANT simulation.

8.1 Conclusion

The purpose of this diploma work was to measure the absolute efficiency of a NE-213 liquid scintillator and to measure the transmission of neutrons through a veto detector. As written in chapter 1, these two detectors played important roles in the ^{4}He(γ,n) experiment carried out at Max-Lab in 1995.

This work thus shows that the evaluaters of the ^{4}He(γ,n) experiment can be confident in using Stanton code calculations and the GEANT simulations, which thus in the end should reveal the charge symmetric nature of the nuclear force.

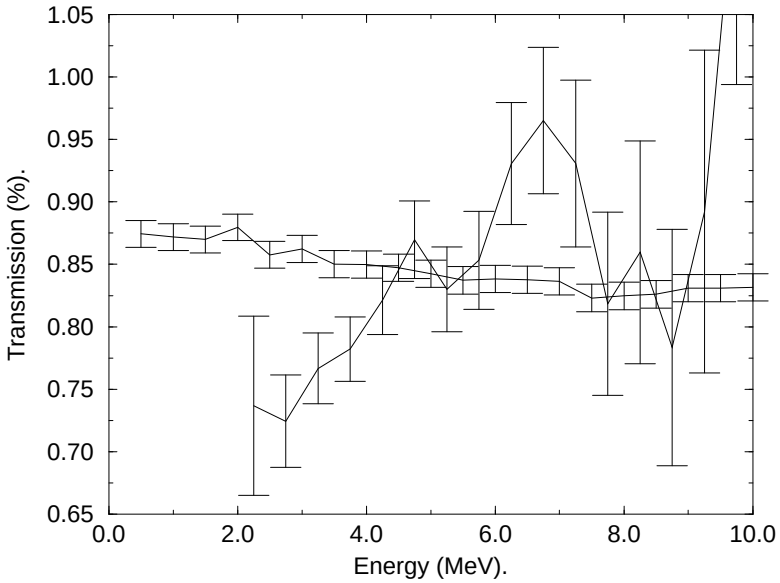

Figure 8.2: Comparison between measured veto transmission and calculated using GEANT, provided by Nilsson [Nil 97]. Besides the statistical error bars the GEANT calculation is believed to have a systematic error of $\sim$5 %.

Chapter 9

Acknowledgements

This work would not have been possible without my supervisor David Sims and my supersupervisor Bent Schrøder, to whom I am truly greatful for all their support. The rest of the kfoto group are of course also recognized, as is Patrik H Ernby.

Appendix A

Data on ^{252}Cf

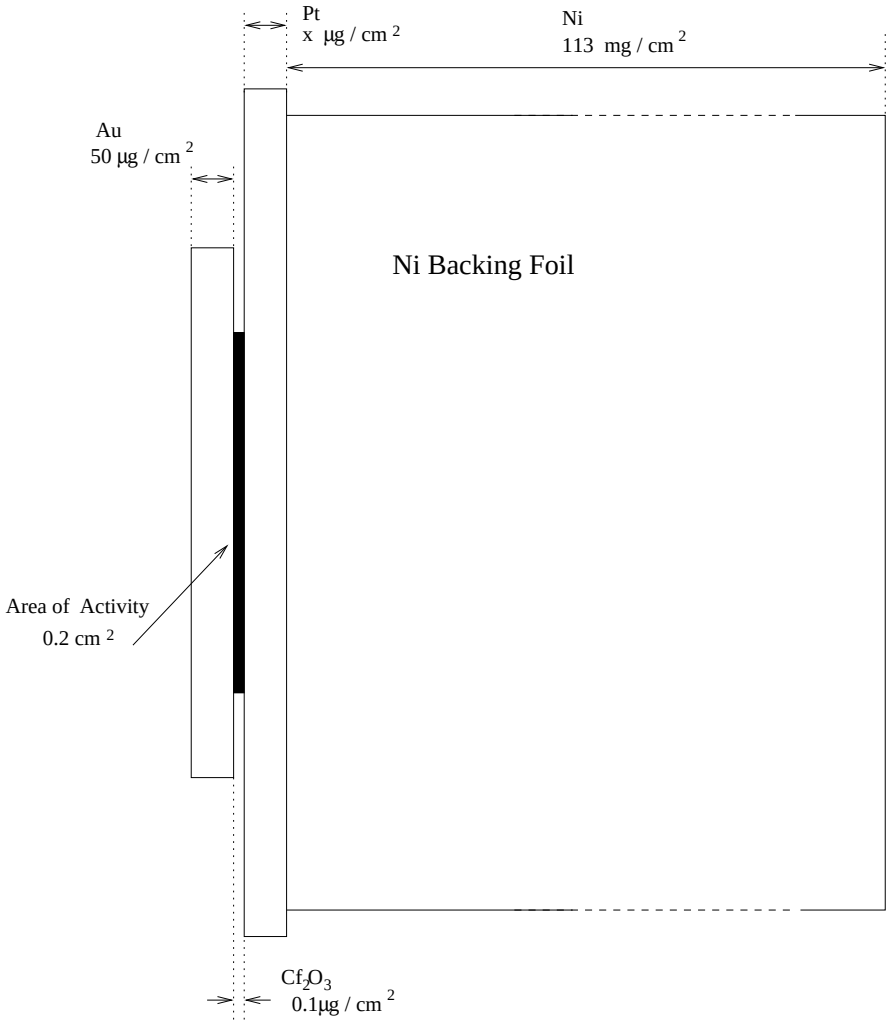

Figure A.1: Schematic figure of the source showing, starting from the left: Gold layer, Activity, Platinium layer and Nickel Backing Foil.

Table A.1: Extract from Table of Isotopes [Tab 78].

$^{252}_{98}Cf$

Δ: 76.031 6 {ANDT 19 175(77)}
σ_c: 20 2 {PC77 Holden}
σ_f: 32 4 (subcadmium) {PC77 Holden}
Ψ: α 96.908%, SF 3.092 6% {Atya 28 361(70)}; β stable {JINC 7 305(58)}; **others:** {NKar 8 63(71), NP A121 433(68), JINC 27 33(65), NIM 14 318(61), PR 107 1635(57), PR 96 1576(54), PR 94 1081(54)}
$t_{1/2}$: 2.646 4 y {JINC 27 33(65)}; 2.637 5 y {Atya 40 174(76)}; 2.638 7 y {NSEg 53 326(74)}; 2.621 6 y {INCL 5 699(69)}; **others:** {IIso 24 185(73), INCL 5 111(69), PR 107 1635(57), PR 102 180(56), PR 96 1576(54), PR 94 1081(54)}
Class: A; **Ident:** chem {PR 93 908(54), PR 94 1081(54)}; chem, mass spect {PR 93 1428(54), PR 96 1576(54), PR 94 1083(54)}
Prod: multiple n-capt from ^{238}U, ^{239}Pu, ^{244}Cm, etc. {PR 93 257(54), PR 94 1083(54), PR 96 1576(54), PR 102 180(56), Bk64 Hyde2}
α: α_0 **6.1183** 5 (†84.0), α_{43} **6.0757** 5 (†15.8), α_{144} **5.9766** (†0.2), α_{297} **5.8263** (†0.002), α_{510} **5.616** (†≈6×10^{-5}) *mag* {YadF 14 1101(71), YadF 11 701(70), YadF 10 1110(69)}
others: {UCRL-11028(63), UCRL-8369 27(58), PR 107 1635(57), PR 100 137(55), PR 96 1576(54)}
γ with α: ⟨**norm:** $\gamma_{0.043}$ (γ 0.0153 7%), from level scheme⟩ Cm $L_{\alpha 1}X$ (†$_\gamma$1.06 7), Cm $L_{\alpha 2}X$ (†$_\gamma$0.120 9), Cm $L_{\beta 1}X$ (†$_\gamma$1.0), Cm $L_{\beta 2}X$ (†$_\gamma$0.238 6), **0.043399** 25 (†$_\gamma$0.00584 40, γ/α 0.0153 9, e/γ 1012 70) *Si(Li)* {NP A178 201(71)}
0.0433 2, **0.1002** 4 *mag conv* {PC64 Asaro2}
0.0434 1 *mag conv* {PR 103 1590(56)}
0.160 15 (γ 0.0020 6%) *scint-semicond γa coinc* {UCRL-11028(63)}
Cm KX (γ 0.007%), **0.042** (γ 0.014%), **0.100** (γ 0.013%) *scint, scint-scint γa coinc* {PR 100 137(55)}
$t_{1/2}$(0.046): 936 ps *Coulomb excit* {PRL 27 1232(71), EB}

Appendix B

Experimental setup

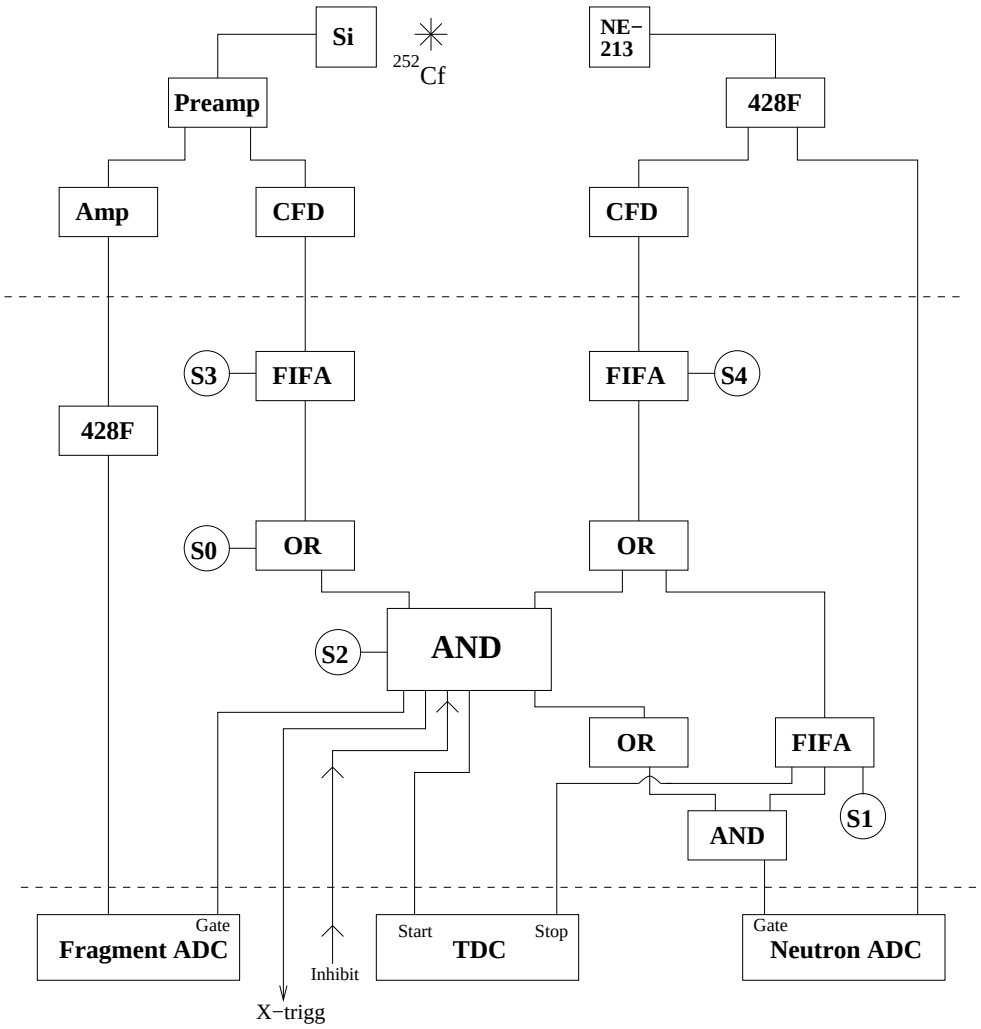

Figure B.1: Experimental setup, delay modules omitted for clarity.

B.1 Listing of the experimental setup

- **NE-213**: NE-213 Liquid Scintillator, 20 cm x 20 cm x 10 cm (hxwxd).
- **Si**: EG & G Ortec F-series heavy ion partially depleted silicon barrier detector.
- **Preamp**: EG & G Ortec Model 142B Preamplifier.
- **Amp**: EG & G Ortec Model 571 Amplifier.
- **CFD**: EG & G Ortec 935 Quad 200 MHz Constant Fraction Discriminator.
- **428F**: LeCroy Linear FAN-IN/FAN-OUT Model 428F.
- **FIFA**: LeCroy Logic FAN-IN/FAN-OUT Model 429A.
- **AND/OR**: LeCroy Quad 2 Input Logic Unit Model 622.
- **Fragment ADC**: LeCroy Peak Sensing ADC Model 2259B.
- **Neutron ADC**: LeCroy Charge ADC Model 2249A.
- **TDC**: LeCroy TDC Model 2228A.
- **S0...S4**: LeCroy Scaler Model 2551.

Bibliography

[Ada 78] J. M. Adams et al., Nucl. Instr. and Meth., **156** (1978) 459.

[And 94] B.-E. Andersson, PhD thesis, University of Lund, Sweden, (1994).

[Arn 89] K. Arnold et al., Nucl. Phys., **A502** (1989) 325c.

[Ato 82] "Atomic Data and Nuclear DataTables", **27**, number 4/4 (1982).

[Bir 64] J. B. Birks, "The Theory and Practice of Scintillation Counting", Pergamon Press (1964).

[Bol 85] J. W Boldeman and M. G. Hines, Nucl. Sci. Eng., **91** (1985) 114.

[Bow 62] H. R. Bowman et al., Phys. Rev., **126** (1962) 2120.

[Bru 82] G. S. Brunson Jr., "Multiplicity and correlated Energy of Gamma Rays Emitted in the Spontaneous Fission of Californium-252", LA-9408-T, Los Alamos National Laboratory (1982).

[Bud 88] C. Budtz-Jørgensen and H. H. Knitter, Nucl. Phys., **A490** (1988) 307.

[Cec 79] R. A. Cecil et al., Nucl. Instr. and Meth., **161** (1979) 439.

[Dro 72] M. Drosg, Nucl. Instr. and Meth., **105** (1972) 573.

[Ede 72] R. M. Edelstein et al., Nucl. Instr. and Meth., **100** (1972) 355.

[Fin 74] E. Finckh, "Nuclear Spectroscopy and Reactions, Part B", Edited by J. Cerny, Academic Press (1974).

[Fow 80] J. L. Fowler et al., Nucl. Instr. and Meth., **175** (1980) 449.

[Fra 52] J. S. Frasern, Phys. Rev., **88** (1952) 336.

[Frö 90] F. H. Fröner, Nucl. Sci. Eng., **106** (1990) 345.

[Gui 97] Guinnes Rekordbok, Forum, (1997).

[Gul 89] K. Gul et al., Nucl. Instr. and Meth., **A278** (1989) 470.

[Han 75] Handbook of Chemistry and Physics, 55th edition, CRC-Press, (1975).

[Hop 71] J. C. Hopkins and G. Breit, Nucl. Data Sect., **A9** (1971) 137.

[Hui 73] J. R. Huizenga and R. Vandenbosch, "Nuclear Fission", Academic Press (1973).

[IAEA 86] "Proc. Advisory Group Mtg. Properties of Neutron Sources", IAEA-TECDOC-410, International Atomic Energy Agency (1987).

[Kno 72] H.H. Knox and T. G. Miller, Nucl. Instr. and Meth., **101** (1972) 519.

[Kno 89] G. F. Knoll, "Radiation Detection and Measurement", 2nd Edition, Wiley (1989).

[Mär 90] H. Märten et al., Nucl. Sci. Eng., **106** (1990) 353.

[MAX 95] "MAX-LAB Activity Report 1995", Edited by J. N. Andersen et al., KFS (1995).

[Mcn 75] M. W. McNaughton et al., Nucl. Instr. and Meth., **116** (1975) 241.

[Nil 97] B. Nilsson, private communication, (1997).

[Nuc Ent] "Scintillators For The Physical Sciences", Brochure from Nuclear Enterprises Limited.

[San 97] A Sandell, private communication, (1997).

[Sch 66] S. Schwarz and H. O. Zetterström, Nucl. Instr. and Meth., **44** (1966) 93.

[Sta 71] N. R. Stanton, COO-1545-92, (February 1971).

[Sim 97] D. A. Sims, private communication, (1997).

[Tab 78] "Table of Isotopes", seventh edition, Edited by C. M. Lederer et al., Wiley (1978).

[Ver 68] V. V. Verbinski et al., Nucl. Instr. and Meth., **65** (1968) 8.